JOURNAL OF GEOPHYSICAL RESEARCH, VOL. 105, NO. A12, PAGES 27,195–27,215, DECEMBER 1, 2000

Improved solar Lyman α irradiance modeling from 1947 through 1999 based on UARS observations

Thomas N. Woods,[1] W. Kent Tobiska,[2] Gary J. Rottman,[1] and John R. Worden[3]

Abstract. The solar Lyman α radiation is the brightest solar vacuum ultraviolet (VUV: λ < 200 nm) emission, and this radiation is deposited in Earth's atmosphere above 70 km. The Lyman α irradiance and its variability are therefore important for many studies of the Earth's upper atmosphere. A long-term data set of the solar Lyman α irradiance from 1947 through 1999 is constructed using the measurements from the Atmospheric Explorer E (AE-E), the Solar Mesospheric Explorer (SME), and the Upper Atmosphere Research Satellite (UARS) along with predictions from proxy models to fill in data gaps and to extrapolate back to 1947. The UARS measurement is used as the reference, and the AE-E and SME measurements and the proxy models are adjusted to agree with the UARS values. The estimated 1-σ uncertainty for this long-term Lyman α time series is 10%. The average solar rotation (27-day) variability in Lyman α is 9% from this composite times series, and the solar rotation variability averaged over 2 years at solar minimum and maximum conditions is 5 and 11%, respectively. The average solar cycle (11-year) variability is a factor of 1.5 when the data are smoothed over 2 years, and the extreme Lyman α variability is a factor of 2.1. The Lyman α irradiances averaged over 2 years during solar minimum and maximum conditions are 3.7 and 5.6 x 10^{11} photons s^{-1} cm^{-2}, respectively. The proxy models include three components to better fit the UARS measurements; nonetheless, there remain differences between the proxy models and the observed Lyman α irradiance, which are related to the source of the Lyman α radiation being different than that for the proxies. The available proxies are primarily chromospheric and coronal emissions, whereas the Lyman α variability is manifested more in the transition region. It is shown that emissions throughout the chromosphere, transition region, and corona vary differently mainly because their contrasts for active network and plage components are different. A transition region proxy is needed to improve the empirical proxy models of solar irradiance, and this composite Lyman α time series could serve as a proxy for other transition region emissions.

1. Introduction

The bright solar Lyman α radiation of the hydrogen emission at 121.6 nm is an important ultraviolet (UV) source of energy throughout the solar system. For the Earth the solar Lyman α photons penetrate into the mesosphere and deposit their energy mainly by molecular oxygen dissociation in the 70-100 km region. In addition, the solar Lyman α radiation dissociates water in the mesosphere and ionizes nitric oxide to form the ionospheric *D* layer between 80 and 110 km. Because the solar Lyman α radiation is the dominant component in the solar spectrum to drive atmospheric changes in the 70-110 km region, it plays an important role in the chemistry of the minor species such as water vapor, ozone, and nitric oxide [*Frederick*, 1977; *Brasseur and Simon*, 1981]. Therefore accurate measurements of the solar Lyman α irradiance are important for studies of the ionosphere and mesospheric chemistry.

The determination of the hydrogen density in the heliosphere, comets, and planetary atmospheres is largely based on measuring the brightness at Lyman α caused by the resonant scattering of the solar Lyman α emission. In particular, the column density of hydrogen is derived by dividing the measured brightness of the H I Lyman α emission by the g factor, or fluorescence efficiency, and the g factor is based on well-known atomic parameters, such as the emission's oscillator strength, and the solar irradiance [*Meier*, 1995]. Consequently, the accuracy of the hydrogen abundance is directly dependent on the accuracy of the Lyman α brightness measurement and on the accuracy of the solar Lyman α irradiance, both intensity and line profile. Often there are not correlative measurements of the solar Lyman α irradiance, so estimates or measurements at different times are instead used to analyze the hydrogen abundance in these solar system studies. The long-term, continuous time series of Lyman α irradiance presented here will address this issue by providing accurate solar Lyman α irradiances since 1947, at about the time when space-based measurements of the H I Lyman α emissions within the solar system began.

In order to make a long-term time series of the solar Lyman α irradiance, models of the Lyman α irradiance are needed for time periods when measurements are not available. Understanding the sources of the Lyman α radiation is important for developing accurate models of the Lyman α irradiance. The Lyman α irradiance has both chromospheric and transition region sources [*Vernazza et al.*, 1981], and the

[1]Laboratory for Atmospheric and Space Physics, University of Colorado, Boulder.
[2]Federal Data Corporation, Jet Propulsion Laboratory, Pasadena, California.
[3]Atmospheric and Environmental Research Inc., Cambridge, Massachusetts.

Paper number 2000JA000051.
0148-0227/00/2000JA000051$09.00

radiative process of this emission complicates the emergence of the Lyman α radiation. The main component of Lyman α irradiance is the central 0.1 nm line core, which is formed at a temperature of ~40,000 K in the transition region [*Fontenla et al.*, 1991]. The Lyman α line width of 0.1 nm is due to radiative damping, the Stark effect (electric field broadening), and resonance broadening [*Roussel-Dupré*, 1983; *Vernazza et al.*, 1981]. The transition region Lyman α core emission, besides contributing to the irradiance output, radiates down into the chromosphere where coherent scattering leads to partial redistribution of the Lyman α radiation into broad wings [*Roussel-Dupré*, 1983; *Vernazza et al.*, 1981]. The source of the Lyman α wing goes deeper into the chromosphere as one observes farther from the line center. The source function for the Lyman α emission as calculated by *Fontenla et al.'s* [1991] model is presented by *Woods et al.* [1995]. The source function for the quiet Sun model (model C-average cell interior) has the peak Lyman α emission near 40,000 K in the lower transition region. For the plage model (model P), the Lyman α source function has its peak higher in the transition region at a temperature of ~70,000 K and accompanied by an increase in the radiance by a factor of ~6. This shift of the source function to higher in the transition region for plages is probably the main reason why the Lyman α irradiance varies more like a transition region emission than like a chromospheric emission.

Recent progress to consolidate the past solar Lyman α irradiance measurements into a long-term composite time series includes the effort of *Woods and Rottman* [1997] and *Tobiska et al.* [1997]. These previous results only included UARS Solar Stellar Irradiance Comparison Experiment (SOLSTICE) data through 1994, which is almost 2 years before the recent solar minimum. The new results presented here include both solar cycle minimum and maximum measurements by the UARS SOLSTICE, significant improvements to the UARS SOLSTICE data processing, and a composite time series of Lyman α irradiance that fills the measurement gaps and extends the time series back almost 30 years further than the previous estimates. The improvements to the UARS SOLSTICE Lyman α irradiances are presented first, followed by the proxy models of the Lyman α irradiance that are calibrated to the UARS solar data. Then the composite of the revised measurements and proxy model predictions is presented as a single, consistent time series of the Lyman α irradiance from 1947 through 1999 with no data gaps. Finally, the sources of the Lyman α emission and of the proxies are examined in order to interpret the differences seen between the Lyman α and proxies variability.

2. Lyman α Measurements

Because of the atmospheric absorption, the solar Lyman α radiation must be measured from space. Several satellites have measured the solar Lyman α irradiance: Solrad 8 (1966), Orbiting Solar Observatory 3 (OSO 3: 1967), OSO 4 (1967-1968), OSO 5 (1969-1975), OSO 6 (1969-1970), Nimbus 3 and 4 (1969-1973), Atmospheric Explorer E (AE-E: 1977-1980), Solar Mesospheric Explorer (SME: 1981-1989), San Marco (1988), and Upper Atmosphere Research Satellite (UARS: 1991-2000). There have also been over 60 sounding rocket measurements of solar Lyman α since 1949; many of these rocket experiments were from the Air Force Geophysical Laboratory (now Phillips Laboratory), the Naval Research Laboratory, and the University of Colorado to provide an underflight calibration for the satellite measurements. Despite the underflight calibration effort, the satellite measurements of the solar Lyman α irradiance do have significant differences. These differences are partly due to using different photometric standards and to having limited on-board calibration for the pre-UARS solar instruments. Resolving these differences is important in order to combine the different data sets into a single reference and thereby to estimate long-term solar variability.

The satellite measurements used here are from the AE-E, SME, and UARS. The uncertainties for the SME Lyman α irradiances are ~40% [*Rottman*, 1981; *Mount and Rottman*, 1983], and the uncertainties for the AE-E Lyman α irradiances are ~30% [*Hinteregger et al.*, 1981]. Whereas, the uncertainty for the UARS Lyman α irradiance is 5% [*Woods et al.*, 1996]. The SME and AE-E measurements could therefore be adjusted within their respective uncertainty levels to agree with the UARS values. These uncertainties and others used elsewhere in this report are 1-σ values.

Because these three satellite missions do not overlap in time, the adjustments for the AE-E and SME data must be determined using proxy models of the Lyman α irradiance that are scaled to the UARS solar measurements. *Woods and Rottman* [1997] used proxy models involving the Penticton (Ottawa) 10.7-cm radio flux ($F10.7$) [*Tapping*, 1987], the National Oceanic and Atmospheric Administration (NOAA) Mg II core-to-wing ratio (Mg C/W) [*Heath and Schlesinger*, 1986; *Donnelly et al.*, 1994], the National Solar Observatory (NSO) He 1083-nm equivalent width (He EW) [*Harvey and Livingston*, 1992], and the Pioneer Venus (PV) Langmuir probe solar measurements (Ipe) [*Hoegy et al.*, 1993]. *Tobiska et al.* [1997] used a proxy model derived from the Lyman α sky background measurements made over two solar cycles by the PV Orbiter Ultraviolet Spectrometer (PVOUVS). The AE-E and SME adjustments from *Woods and Rottman* [1997] and from *Tobiska et al.* [1997] are very similar. Their differences arise primarily in the data chosen as the UARS Lyman α irradiance reference value. *Tobiska et al.* [1997] chose to use the measurements solely from the UARS SOLSTICE [*Rottman et al.*, 1993]. *Woods and Rottman* [1997] also used the SOLSTICE Lyman α values but modified by a factor of 0.95 to represent an average of the measurements from the two UARS instruments, SOLSTICE and Solar Ultraviolet Spectral Irradiance Monitor (SUSIM) [*Brueckner et al.*, 1993]. The 10% difference between the UARS SOLSTICE and UARS SUSIM Lyman α irradiances is within their 2-σ absolute uncertainty of 10% [*Woods et al.*, 1996].

The previous studies by *Woods and Rottman* [1997] and *Tobiska et al.* [1997] considered data only during the declining phase of solar cycle 22. This new analysis extends from solar cycle 22 maximum through solar minimum and into the rising phase of solar cycle 23. Consequently, the longer time period, coupled with improvements to the UARS SOLSTICE data processing algorithms and calibration parameters, prescribes different scaling factors for the AE-E and SME Lyman α irradiances.

For the long-term composite Lyman α time series presented here, the UARS SOLSTICE version 13 Lyman α irradiances are chosen as the reference. The differences between the UARS SUSIM (version 19) and SOLSTICE Lyman α irradiances are now only a few percent as shown in Figure 1. Prior to 1993 the SOLSTICE values are, on average, 2% lower than the

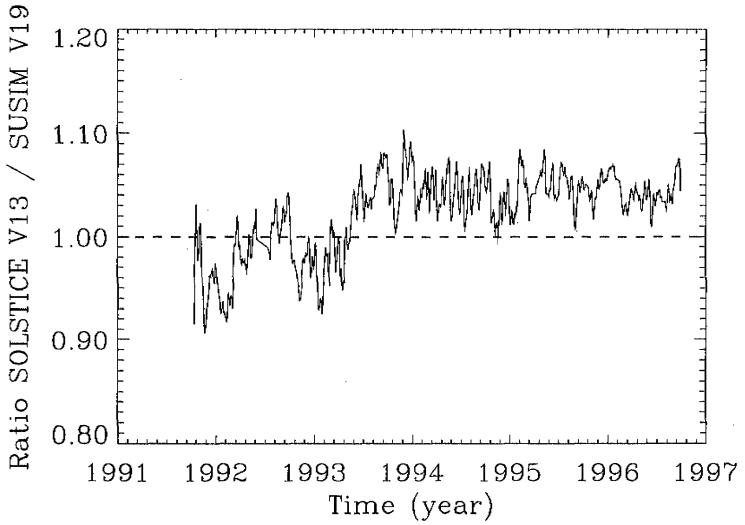

Figure 1. Solar Ultraviolet Spectral Irradiance Monitor (SUSIM) – SOLar STellar Irradiance Comparison Experiment (SOLSTICE) Lyman α comparison. The average ratio changes from 0.98 to 1.04 during 1993.

SUSIM values. After 1993 the SOLSTICE values are, on average, 4% higher than the SUSIM values. These differences are instrument and calibration artifacts. We considered using the average of SUSIM and SOLSTICE data as the reference but decided that the reference time series would be more consistent using data from a single instrument. As compared to a factor of 2 for solar cycle variability, the differences of a few percent between SOLSTICE and SUSIM would not significantly alter the results presented here.

An important difference between this new composite Lyman α time series and *Woods and Rottman*'s [1997] and *Tobiska et al.'s* [1997] time series is that the SOLSTICE version 13 data products are now used. The two previous results used the SOLSTICE version 9 data products. The SOLSTICE version 13 data processing software has several algorithm enhancements. The four algorithm changes that affect the Lyman α irradiance the most are (1) a new, time-dependent, wavelength-scale correction, (2) a new, time-dependent, field of view (FOV) correction, (3) an improved, overflow counter correction, and (4) an improved algorithm to calculate the line integral. The ratio of the SOLSTICE Lyman α version 9 to version 13 is shown in Figure 2. The primary difference is from the new wavelength-scale correction. The second most important improvement is from the new FOV correction. The improved overflow counter correction reduces day-to-day noise but does not contribute to the long-term

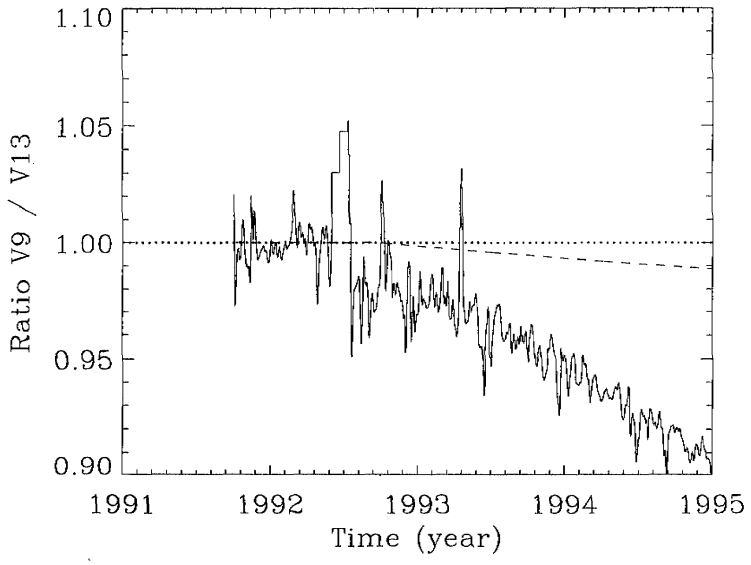

Figure 2. Comparison of SOLSTICE Lyman α version 9 to version 13. The dashed line is the new field of view correction. The remaining difference is primary from the new wavelength-scale correction.

trend. The new line integral algorithm improves the accuracy of deriving the irradiance into 1-nm intervals, but it does not contribute to the long-term trend.

The new wavelength-scale correction is needed to account for a slow drift of the SOLSTICE grating drive encoder electronics. This encoder degradation was first discovered from examination of changes in solar line widths; some were slowly growing wider, and some were slowly growing narrower. Through the comparisons of daily spectra to a reference solar spectrum early in the UARS mission, the grating drive encoder signal was found to be slowly drifting, and a simple correction for the encoder degradation is now applied. The new wavelength-scale correction algorithm has yielded line widths that remain constant over the mission. This wavelength-scale correction is the most significant improvement over the previous work as it affected the long-term trend by several percent.

The FOV correction is a new calibration for the "hole" seen in the SOLSTICE G channel (119-180 nm) FOV maps [*Woods et al.*, 1999]. This FOV correction is largest for the longer wavelengths of the G channel; nevertheless, this correction is also important for the SOLSTICE Lyman α time series. The FOV correction for Lyman α is about a 1-2% correction and is shown in Figure 2 as the dashed line.

The improvements in the overflow counter correction algorithm, which is used when detector counts exceed the 16-bit hardware counter, has yielded lower day-to-day noise in the SOLSTICE Lyman α time series.

The fourth algorithm improvement is the change from a numerical integration to an analytical integration using basis spline functions fitted to the data [*Lawson and Hanson*, 1974; *de Boor*, 1978]. The basis spline integrations are done for both the line integrations, such as for the Lyman α emission, and the 1-nm intervals used in the UARS Level 3BS data products. The use of analytical integrations has improved the accuracy of creating 1-nm intervals for the SOLSTICE Level 3BS data product. With the old numerical integration algorithm, there were differences of a few percent between the Lyman α irradiance represented by the 121-122 nm interval irradiance and the irradiance from a Gaussian fit to the Lyman α line. Now the Lyman α irradiances extracted the two different ways are in agreement using the new analytical integration algorithm.

3. Lyman α Proxy Models

Models of solar irradiance are used primarily for atmospheric studies for time periods when measurements are not available. A commonly used solar irradiance model for upper atmospheric studies is *Hinteregger et al.*'s [1981] proxy model. This model and other proxy models employ empirically derived relationships of solar irradiance at one wavelength relative to an index of solar variability that is available on an almost daily basis over many years. Improvements in modeling the solar Lyman α irradiance variability can be obtained by specifying the irradiance as a function of the distribution of quiet and magnetic solar surface features, such as was done by *Lean and Skumanich* [1983] and *Worden* [1996]. Both of their models parameterize the solar irradiance as three components: quiet Sun, active network, and plage areas whereby the areas of each component are derived from Ca II K solar images. A more detailed description of these three components and the relationship of these components to the empirical proxy models is given in section 6. A more physical model of the Lyman α irradiance is the radiative transfer calculations using semiempirical models of the solar atmospheric structure (density and temperature), such as those by *Vernazza et al.* [1981] and *Fontenla et al.* [1999]. In *Fontenla et al.'s* [1999] model, solar images are used to identify seven components of the solar atmosphere (e.g., cell interior, network, and plage), and then an emission's source function is calculated using seven static models of the solar atmosphere. However, the image analyses have only been done over a limited time period and thus are difficult to extend back to the time of the AE-E mission and before. Therefore the simpler proxy model approach is applied here but with some improvements over previous proxy models.

The validity of a proxy model is strongly dependent on the validity of the proxy over its entire time range and on the physical processes connecting the proxy emission and the Lyman α emission within the solar atmosphere. The Lyman α radiation is formed in the chromosphere and transition region of the solar atmosphere, so the most appropriate solar proxies should likewise have a dominant contribution from these regions. In addition, the time series of the proxies need to be long enough to overlap AE-E, SME, and UARS. The three indices used here for Lyman α proxy modeling are the $F10.7$, Mg C/W, and He EW. The solar $F10.7$ measurement has the longest duration dating back to 1947. The two primary sources in the solar atmosphere for the 10.7-cm radio flux are the free-free electron emission (bremsstrahlung) throughout the chromosphere, transition region, and lower corona and gyroresonant absorption in strong magnetic fields in the transition region and corona [*Tapping*, 1987]. While the daily $F10.7$ is better correlated with coronal emissions than with the Lyman α emission, both the 81-day average $F10.7$ and the square root of $F10.7$ have a good correlation with the Lyman α emission, better than 0.95. Because the correlation with the square root of $F10.7$ is better than the correlation with $F10.7$, the square root of $F10.7$ is used here solely as an empirical improvement. The He EW measurement is representative of the chromosphere and transition region but is also sensitive to coronal holes. The Mg C/W is representative of the chromosphere.

The empirical fits of the UARS Lyman α irradiance measurements to the three solar indices yield the following models for the solar Lyman α irradiance:

$$E = A + C_L P_{81} + C_S \left(P - P_{81}\right), \quad \text{(1a)}$$

$$E_{He} = 1.1764 + 0.05668\, He_{81} + 0.04032 \left(He - He_{81}\right), \quad \text{(1b)}$$

$$E_{Mg} = -31.68 + 133.7\, Mg_{81} + 79.52 \left(Mg - Mg_{81}\right), \quad \text{(1c)}$$

$$E_{F10} = 0.5839 + 0.3554 \sqrt{F10_{81}} + 0.1730 \left(\sqrt{F10} - \sqrt{F10_{81}}\right). \quad \text{(1d)}$$

The proxy variables P are labeled He for the NSO He-1083 nm EW, Mg for the NOAA Mg II core-to-wing ratio, and $\sqrt{F10}$ for the square root of $F10.7$. The irradiance E is given in units of 10^{11} photons s^{-1} cm^{-2}. The variables, or indices, with the "81" subscript are the daily proxy values smoothed over a period of 81 days. Data gaps in the proxies, which pose a problem for the 81-day smoothing function, are filled by interpolation if the gap is smaller than 6 days or by fast Fourier transform analysis if the gap is larger [*Worden*, 1996]. These proxy models are derived empirically using the common method of multiple linear regression. The SOLSTICE Mg II core-to-wing ratio is also used for analysis later, and the SOLSTICE Mg

proxy is related to the NOAA Mg proxy as $Mg_{NOAA} = 0.1914 + 0.3787\ Mg_{SOLSTICE}$. The three terms in (1) represent a constant term (conceptually, the quiet Sun), long-term variation, and short-term variation. The third coefficient, C_S, is the sensitivity to the short-term variation, predominantly from 27-day solar rotation. Likewise, the second coefficient, C_L, is the sensitivity to the long-term variation. *Lean and Skumanich* [1983] and *Worden* [1996] have shown for chromospheric emissions that the short-term variation is due mostly to plage modulated by solar rotation and that the long-term variation is due mostly to variations in both plages and active network. These simple three-component proxy models were motivated by the more physical three-component models of irradiance variability by *Lean and Skumanich* [1983] and *Worden* [1996] in which they used Ca II K images to derive plage and active network areas as the main variables in their models. The quiet Sun (solar minimum) irradiance from (1) is 3.55 x 10^{11} photons s^{-1} cm^{-2} using the 81-day-smoothed solar minimum values for the proxies: He=He_{81}=42, Mg=Mg_{81}=0.26, and $F10$=$F10_{81}$=70.

These proxy model coefficients are similar to, but consistently different from, the equivalent model coefficients given by *Woods and Rottman* [1997]. Because the new SOLSTICE version 13 Lyman α irradiance has a higher solar minimum value than that extrapolated using SOLSTICE version 9 data, the constant coefficients are higher than those given by *Woods and Rottman* [1997], and the long-term variation coefficients are lower than *Woods and Rottman's* [1997] results. As expected, the 27-day variation coefficients are more consistent with previous results as they are not sensitive to the long-term trend.

As a validation check for these models, we also derive the model parameters for the SOLSTICE Lyman α irradiance over shorter time periods. If the model parameters are consistent by using different SOLSTICE data periods, then one could conclude that the SOLSTICE data set is consistent throughout its mission and that the proxy model is a reasonable representation at different stages of solar variability. The lifetime of a plage decaying into active network is one to three solar rotations [*Foukal*, 1998], and the lifetime of active network diffusing into the quiet network is possibly several solar rotations. So a period of nine solar rotations, 243 days, is chosen for this validation analysis. The three parameters, A, C_L, and C_S, are shown in Figure 3, using the Mg proxy model over a 243-day period every 27 days. These 243-day fitting results indicate that the short-term parameter, C_S, varies 17% over the SOLSTICE mission; however, the constant coefficient, A, and the long-term parameter, C_L, vary 75 and 50%, respectively. *Barth et al.* [1990] found similar variation of the coefficients for a two-component Lyman α model in that the coefficients changed by a factor of 1.6 during different phases of the solar cycle. These 243-day A and C_L

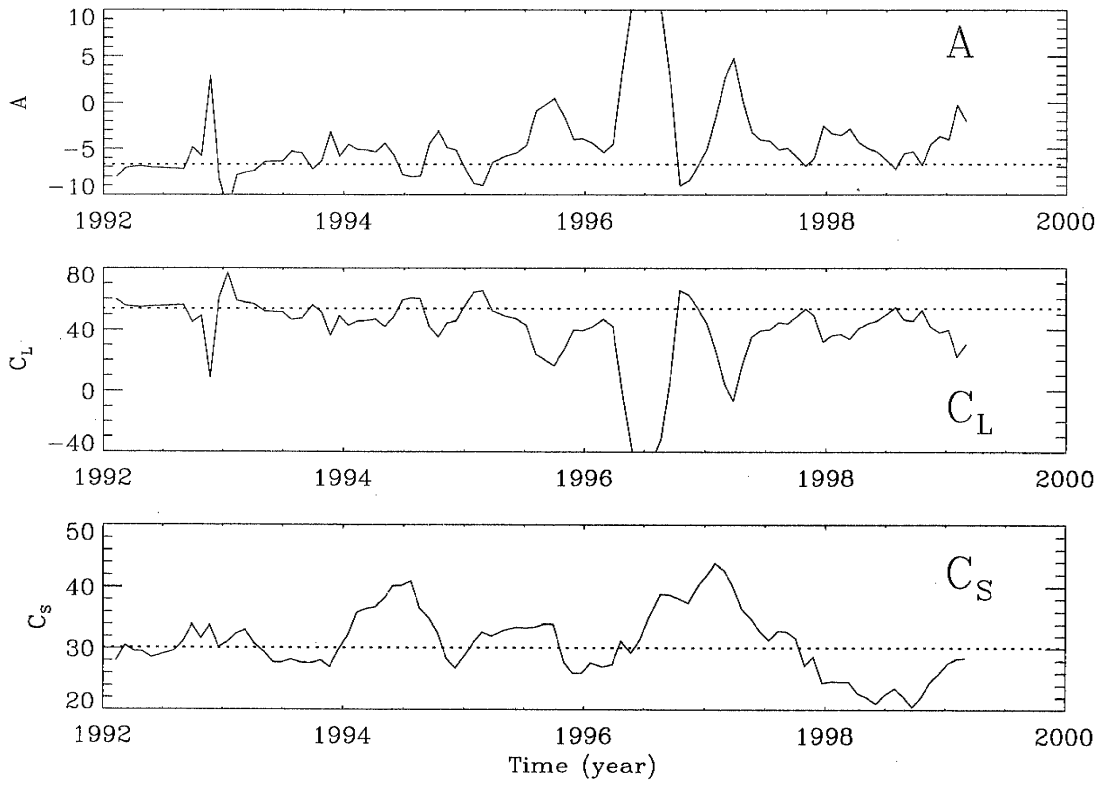

Figure 3. Proxy model parameters for 243-day periods. The parameters for the Mg proxy model are fitted for a 243-day period every 27 days. The times when A and C_L change the most are the times when there is little solar activity or when the solar activity level changed rapidly. The dotted lines are the values for the model parameters using the entire SOLSTICE mission. These values are not the same as equation (1) values because the SOLSTICE Mg core-to-wing ratio (Mg C/W index) is used here instead of the NOAA Mg C/W index.

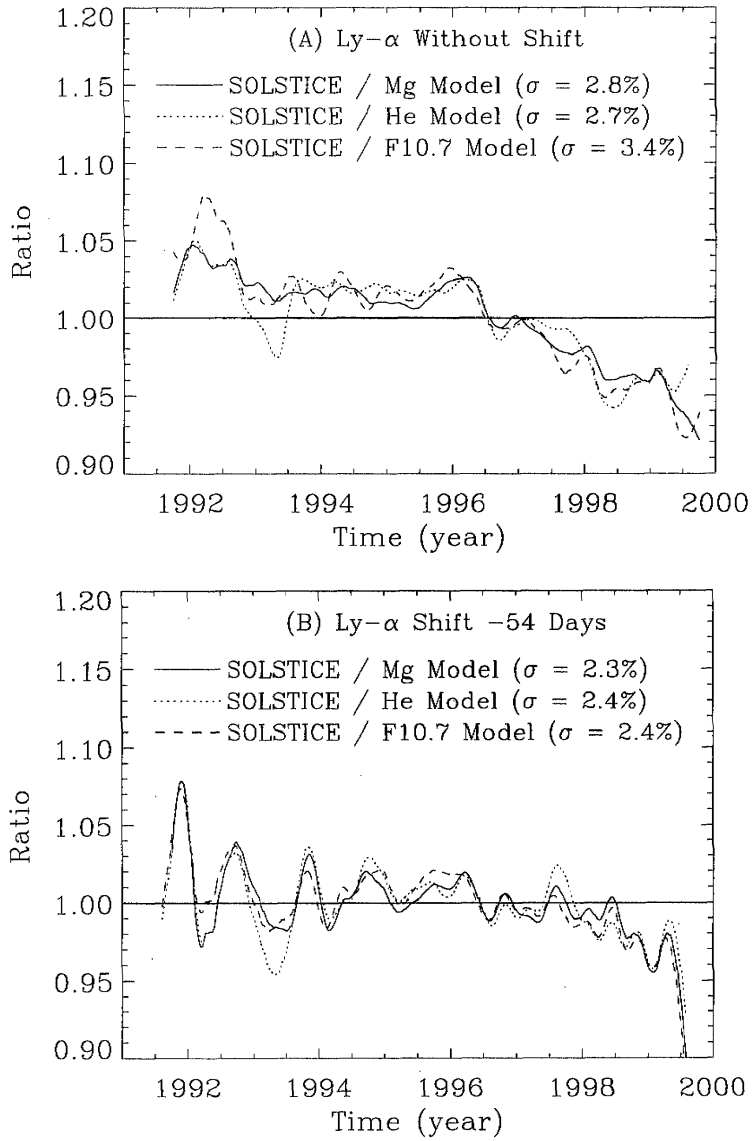

Figure 4. Proxy model comparison for UARS SOLSTICE Lyman α. (a) Model comparisons with no shifts between the proxies and Lyman α. There is a downward trend after solar minimum (1996) for this comparison. (b) Model shows model comparisons with SOLSTICE Lyman α shifted backward (earlier) by 54 days (two solar rotations). The downward trend is reduced with this 54 day shift, and this change is discussed in section 6.5. The standard deviation (σ) of the fit is shown in parentheses.

parameters are consistent with the values derived using the entire SOLSTICE data set (dotted lines in Figure 3). Note that these values are not the same as equation (1) values, because the SOLSTICE Mg C/W index is used here instead of the NOAA Mg C/W index. The times of little solar variability as in 1996 and the times of rapid changes as in 1993 are when the 243-day A and C_L parameters deviate the most from the mean value. The He proxy model shows very similar results when it is analyzed in the same way, but the $F10.7$ proxy model shows a factor of 2 larger spread of the parameters in doing the 243-day fitting. Because the 243-day parameters do not show any long-term trend, there does not appear to be any significant instrument artifacts remaining in the SOLSTICE data set. We also conclude that the Mg and He proxies seem the more appropriate proxies to represent the solar Lyman α variability.

The major limitations for the proxy models are the uncertainties in the proxies themselves, the uncertainties in the solar irradiance data used to derive empirically the model coefficients, and intrinsic differences between the physical regions and mechanisms that emit the radiation for the proxy and at Lyman α. The uncertainties in the proxies are estimated from the day-to-day noise in the proxy and the difference in solar minimum values, assuming that all solar minimum

values should be the same. The day-to-day noise is calculated as the standard deviation of the difference between the proxy and a 3-day-smoothed proxy. This calculation may also include true solar variability, but the value is small anyway. The day-to-day noise is 1.3, 0.3, and 0.9% for He, Mg, and $\sqrt{F10}$, respectively. The difference between the solar minimum values averaged over a year is 6.3, 0.1, and 2.9% for He, Mg, and $\sqrt{F10}$, respectively. The larger difference for the He proxy may be related to the change of the He EW instrument in 1993. Therefore we estimate the proxy uncertainties to be 6, 0.3, and 3% for He, Mg, and $\sqrt{F10}$, respectively. From validation with UARS SUSIM and analysis of the SOLSTICE irradiance algorithms, the uncertainty for the UARS Lyman α irradiance is 5% [*Woods et al.*, 1996]. An estimate for the intrinsic difference between the source region of the index and the source region of Lyman α is the standard deviation (1-σ) of the difference between the model prediction and the UARS measurements, being 2.7, 2.3, and 3.0% for the He, Mg, and $F10$ models, respectively (see Figure 4a). This uncertainty should be considered a lower limit rather than the best approximation for the intrinsic difference between the index and Lyman α source regions. Combining these uncertainties, the expected uncertainty for the proxy model predictions is 8, 6, and 7% for the He, Mg, and $F10$ models, respectively. A validation check on the total uncertainty of the proxy model predictions is the temporal difference, not including the systematic offset, of the model predictions to the SME measurements, being 2.8, 3.2, and 4.0% for the He, Mg, and $F10$ models, respectively (see Figure 5a). Hence an uncertainty of 10% appears reasonable to adopt for the proxy model predictions. While additional analysis or different algorithms might provide a proxy model with an uncertainty better than 10%, the uncertainty of the UARS irradiances will remain the limiting factor for the proxy model uncertainty.

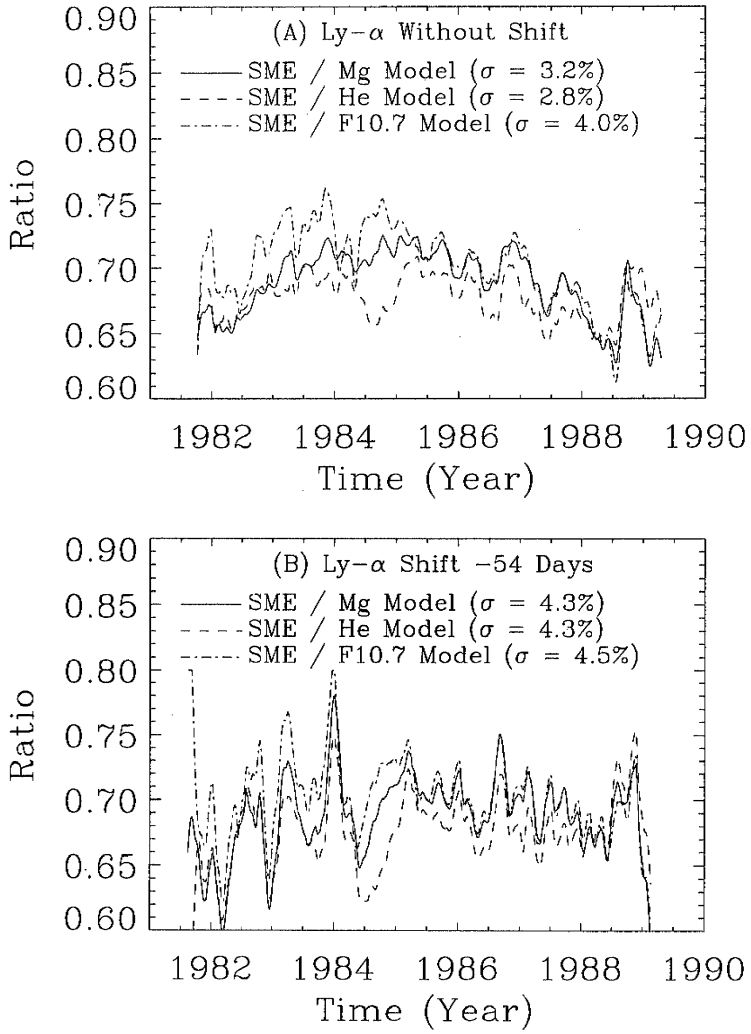

Figure 5. Proxy model comparison for Solar Mesospheric Explorer (SME) Lyman α. (a) Model shows model comparisons with no shifts between the proxies and Lyman α. There is a downward trend after solar minimum (1986) for this comparison. (b) Model shows model comparison with the SME data shifted backward (earlier) by 54 days (two solar rotations). The downward trend is reduced with this 54-day shift, and this change is discussed in section 6.5. The standard deviation (σ) of the fit is shown in parentheses.

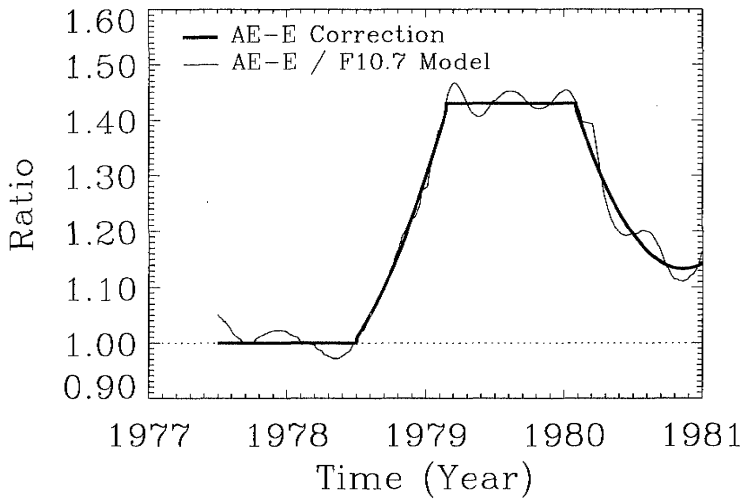

Figure 6. Proxy model comparison for AE-E Lyman α. The correction for the AE-E Lyman α is a time-dependent function shown as the thick line.

Considering that the solar cycle Lyman α variability is about a factor of 2, the proxy model uncertainty of 10% is quite adequate for modeling the long-term solar variability.

4. Composite Lyman α Time Series

A composite Lyman α time series is formed using the UARS SOLSTICE Lyman α measurements, adjusted measurements from AE-E and SME, and proxy model predictions to fill the data gaps and to extend the time series back to 1947. We use the UARS Lyman α data as our fundamental reference both for the absolute registration of this time series in order to establish adjustments for the AE-E and SME data and for the development of the proxy models of the solar Lyman α irradiance.

The scaling factors for the SME and AE-E Lyman α irradiance are derived assuming that the UARS SOLSTICE proxy models are valid and can be extrapolated to times prior to the UARS mission. The average ratios of the SME data to the proxy models shown in Figure 5a are 0.69, 0.68, and 0.70 for the Mg, He, and *F*10.7 models, respectively. The standard deviation for these ratios is only 3%, mainly because the ratios do not have a strong variation with time. Because the degradation of the SME solar instrument is a small correction at Lyman α, this result implies that the SME solar instrument was relatively stable during its mission. A scaling factor of 0.69 that is independent of time is adopted for scaling the SME Lyman α irradiances. This value is the average of the proxy model ratios presented in Figure 5a. The SME Lyman α irradiances, divided by this scaling factor, are increased and become consistent with the SOLSTICE Lyman α irradiance values.

On the other hand, the comparison of the AE-E Lyman α irradiances to the proxy models shows significant variations from the mean difference. *Fukui* [1990] argues that the 1979 anomaly in the AE-E Lyman α irradiances is a real solar effect because two AE-E channels recorded the same variation in the Lyman α irradiances and a similar, but smaller, variation was observed in the AE-E Lyman β emission. While their study and conclusions should not lightly be dismissed, ground-based solar measurements do not suggest an obvious solar mechanism that could explain the 45% anomaly of the AE-E irradiances. From our experience with photomultiplier tube (PMT) detectors, we have seen changes in PMT gain that can both go up or go down as the high-voltage power supply (HVPS) degrades, as the temperature of the HVPS changes, or as the 28-V input supply (battery-solar cells) changes levels. *Fukui* [1990] does not consider these possible effects; nonetheless, these effects would probably have affected other AE-E channels in a similar manner. Another possibility is that the contamination levels changed. *Fukui* [1990] indicates that the AE-E detectors are most sensitive to contamination at Lyman α and longer wavelengths, because the response at Lyman α dropped by a factor of 5 during the first several months of the AE-E mission while the response at shorter wavelengths changed by less than 30%. *Fukui* [1990] speculates that this decrease in Lyman α responsivity is due to outgassing of the photocathode impurities from the detector. Impurities tend to migrate to the colder components, so it is conceivable that some of the impurities could return to the detectors if the detectors were colder during the anomaly period. These ideas are only speculations on how the AE-E instrument might have degraded during the anomaly period. In order for the AE-E Lyman α measurements to be consistent with the proxy models, the AE-E instrument responsivity is assumed, without proof, to change during the anomaly period. Consequently, a time-dependent scaling factor for the AE-E Lyman α irradiances is adopted as shown in Figure 6. These scaling factors, *f*, for the AE-E Lyman α irradiances include constant offsets plus quadratic fits with time, *t*, in fractional years, as listed in (2).

$$1977.5\text{-}1978.5 \qquad f = 1.0 \tag{2a}$$

$$1978.5\text{-}1979.145 \qquad f = 2365.15 - 60.615\,t + 0.38852\,t^2 \tag{2b}$$

$$1979.145\text{-}1980.085 \qquad f = 1.43 \tag{2c}$$

$$1980.085\text{-}1981 \qquad f = 3153.56 - 77.978\,t + 0.48222\,t^2 \tag{2d}$$

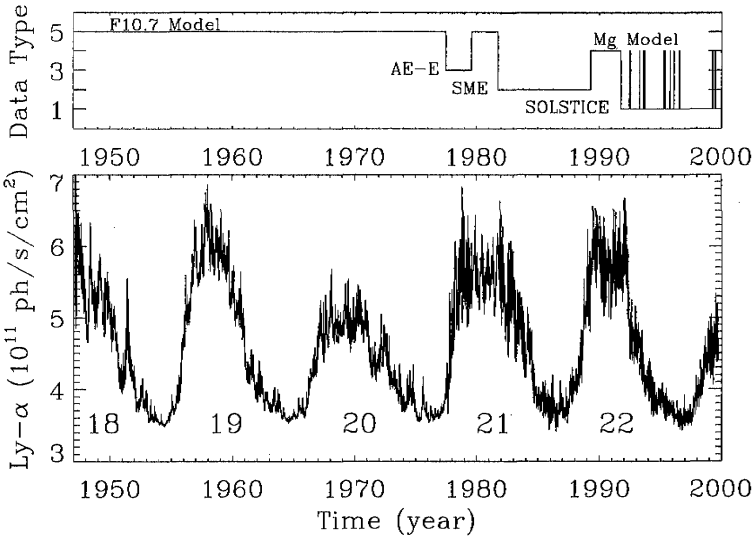

Figure 7. Composite solar Lyman α time series. The top panel shows the source for the Lyman α irradiance shown in the bottom panel. The sources are (1) UARS SOLSTICE, (2) SME, (3) AE-E, (4) Mg proxy model, and (5) *F*10.7 proxy model.

These scaling factors for SME and AE-E are higher than the scaling factors given by *Woods and Rottman* [1997] and *Tobiska et al.* [1997], because the UARS SOLSTICE version 13 Lyman α irradiances have a higher solar minimum value than the extrapolated value from the SOLSTICE version 9 data. Because the UARS mission has now observed both solar maximum and minimum conditions, these scaling factors are not expected to change significantly as the UARS mission extends its solar observations into the next solar cycle.

The composite Lyman α time series is shown in Figure 7 along with an indicator of the source of the values in the time series: (1) UARS SOLSTICE Lyman α measurements, (2) scaled SME Lyman α measurements, (3) scaled AE-E Lyman α measurements, (4) Mg II C/W model predictions used between SME and UARS observations and for filling SOLSTICE data gaps, and (5) *F*10.7 model predictions used prior to SME observations. The Mg II C/W proxy is considered the more appropriate proxy for chromospheric emissions, but the *F*10.7 proxy is utilized in order to extend the composite time series back to 1947. For data gaps of less than 5 days the measurements are linearly interpolated to fill the data gaps. For longer data gaps the proxy models are used to fill the data gaps. The composite time series is then smoothed by 3 days to help reduce day-to-day noise and to make transitions smooth from one data source to another.

The many rocket measurements of the solar Lyman α irradiance from 1949 to 1998 serve as a validation for the composite Lyman α time series. The comparison of 59 rocket measurements [*Vidal-Madjar*, 1977; *Mount and Rottman*, 1983, 1985; *Rottman*, 1981; *Van Hoosier et al.*, 1988; *Woods and Rottman*, 1990] to the composite time series is shown in Figure 8. The 42 Lyman α measurements from *Vidal-Madjar*'s [1977] review of the solar Lyman α irradiance are indicated by the asterisks. *Vidal-Madjar* [1977] had concluded that the Lyman α irradiance ranged from 2 to 4 x 10^{11} photons s^{-1} cm^{-2} with an uncertainty of 30%. These earlier rocket measurements, except for one measurement in 1955, do not confirm our composite Lyman α time series. These values are a factor of ~1.7 smaller than our composite Lyman α time series. *Vidal-Madjar* [1977] noted that some atmospheric and cometary studies suggest an increase of the solar extreme ultraviolet (EUV) and Lyman α irradiances by a factor of 2. While our composite Lyman α time series support this factor of 2 increase of *Vidal-Madjar*'s [1977] values, it is difficult to resolve this factor of 2 when both the uncertainty of these solar Lyman α irradiance measurements and the uncertainty of the atmospheric model predictions were estimated at 30% or larger [*Vidal-Madjar*, 1977]. However, there are some concerns about the use of tungsten photodiodes for the calibration of the earlier solar instruments (W. Neupert, private communication, 1993) because *Canfield et al.* [1973] found that the photoelectric yield of tungsten could change by as much as a factor of 2 above 100 nm based on its surface cleanliness and that these older photodiodes could have a variation in sensitivity across the photodiode by as much as 50%. It seems possible that these original calibration tungsten photodiodes were easily contaminated because only oil-based pumps were used in those times. If so, then these earlier solar measurements are expected to have low values. For these older measurements we assume an uncertainty of 80%, being the combination of the typical 30% measurement uncertainty [*Vidal-Madjar*, 1977] and a 50% uncertainty for the possible systematic error of the tungsten photodiode calibrations.

The more recent rocket measurements from 1976 to 1998 provide a better confirmation of our composite Lyman α irradiances. There are eight measurements that agree with our composite Lyman α irradiances, and the other six measurements are more consistent with the lower values reported by *Vidal-Madjar* [1977]. The SME Lyman α irradiance was calibrated to the 1982 rocket measurement, shown as the large diamond in Figure 8; therefore the SME Lyman α values are expected to be lower than the composite time series. The uncertainties of the rocket Lyman α irradiance measurements are estimated to be ~30-40% [*Rottman*, 1981; *Woods and Rottman*, 1990]. There are several

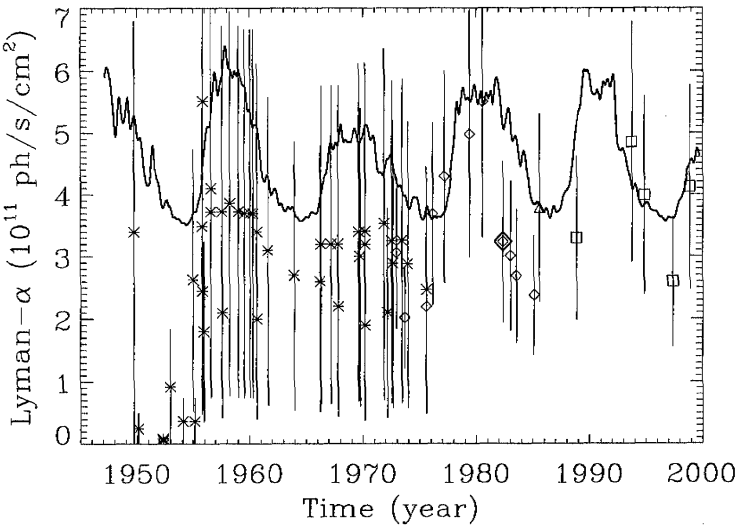

Figure 8. Comparison of rocket Lyman α measurements to smoothed composite time series. The measurements with the asterisks are from the Lyman α review by *Vidal-Madjar* [1977]. These measurements have an uncertainty of ~80%. The measurements with the diamond symbols are from *Rottman* [1981] and *Mount and Rottman* [1983, 1985]. The large diamonds in 1982 highlights the rocket measurement used for calibrating the SME Lyman α measurement. The measurement with the triangle is from *Van Hoosier et al.* [1988]. The other measurements with the squares are results from recent rocket flights by T. Woods and G. Rottman. These measurements since 1975 have an uncertainty of ~40%.

difficulties that we have experienced in calibrating Lyman α instruments that contribute to this fairly large uncertainty. For photon-counting detectors which are often used with spectrometers, there is a large nonlinearity correction for the solar Lyman α data, up to 25% [*Rottman*, 1981]. There is also inconsistency in corrections for scattered light which could affect the results by 10%. The University of Colorado rocket measurements and the SME measurements did not have corrections for scattered light, whereas the UARS SOLSTICE measurements have corrections for scattered light which

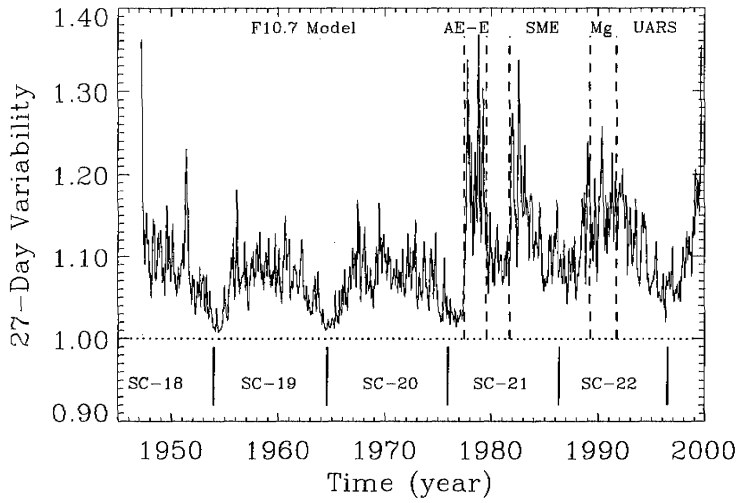

Figure 9. Solar rotation (27-day) variability time series. The ratio of the irradiance maximum to the minimum within a 27-day window is plotted as the 27-day variability. The Lyman α values are taken from the composite time series, and the source of the data is shown in the plot. The *F*10.7 model is also used between the AE-E and SME data sets but is not labeled in the plot. The 27-day variability for the observations is about twice the amount as that for the *F*10.7 model. The 27-day variability for the Mg model is similar to the observation results.

increase the solar Lyman α irradiance. The most recent rocket measurements since 1988 have used nitric oxide (NO) ionization chambers and Si photodiodes with Acton Lyman α filters. The main difficulties with these photometer instruments are that the calibration precision is poor owing to the very low calibration signals, that secondary radiometric standards are used which have higher uncertainties, and that the sensitivity varies by 40% over the detector area for the NO ionization chamber. Considering these many different calibration issues, it is feasible that the rocket Lyman α irradiances have a spread of 60%. It is, however, odd that most measurements seem to fall into either the low group (*Vidal-Madjar* [1977] levels) or the high group (UARS SOLSTICE levels).

5. Lyman α Variability

The ratio of the solar maximum values averaged over 2 years to the solar minimum average is 1.5 ± 0.1, and this ratio represents the typical variation over five solar cycles from this composite time series. The Lyman α irradiances averaged over 2 years during solar minimum and maximum conditions are 3.7 and 5.6 x 10^{11} photons s^{-1} cm^{-2}, respectively. The standard deviations for these values during different solar cycles are 0.05 and 0.39 x 10^{11} photons s^{-1} cm^{-2} for solar minimum and maximum, respectively. The single-day extreme values are 3.4 and 7.1 x 10^{11} photons s^{-1} cm^{-2}, yielding an extreme solar cycle variation of 2.1. *Vidal-Madjar* [1977] had a similar conclusion from data before 1975 in that the solar cycle variation for Lyman α irradiance is a factor of 2.

The variability for solar rotation (27-day) is calculated by taking the ratio of the maximum and minimum within a 27-day window. The range of solar rotation variability in Lyman α is found to be between 1 and 37% as shown in Figure 9. *Vidal-Madjar* [1977] had a similar conclusion from data before 1975 in that the solar rotation (27-day) variation for Lyman α irradiance is no more than 30%. The average solar rotation (27-day) variability is 9 ± 6% over the entire time series. The solar rotation variability for solar maximum and minimum is derived by averaging the 27-day ratios over a 2-year period. The solar rotation variability during solar maximum is 11 ± 5%, slightly larger than the average over the entire time period. The solar rotation variability during solar minimum is 5 ± 3%. When just the observations are considered, the solar rotation variability is 13 ± 7%. The Mg model result is very similar to the observations. However, the *F*10.7 model result is 7 ± 4%, which is almost a factor of 2 lower than the observational result. The *F*10.7 model reproduces the observational long-term irradiance with ~5% accuracy as shown in Figures 3 and 4, but the *F*10.7 model underpredicts the 27-day variability of the observed irradiance by 6-10%. This result indicates that the *F*10.7 model is unable to predict both the long-term and short-term variability with the same accuracy. Another difference between the observations and the *F*10.7 model is that the solar rotation variability during solar minimum conditions is ~5 times higher for the observations. This result also indicates that there is solar activity throughout the solar minimum period for the true Lyman α radiation. Because the 10.7-cm flux remains bright off the solar limb [*Donnelly et al.*, 1983], the 27-day variability of *F*10.7 is expected to be less than the variability for UV emissions. This effect may partially explain why the *F*10.7 model's predictions for the 27-day variability of Lyman α are lower than the observational results throughout the solar cycle. Although the *F*10.7 model reproduces the observations by ~7%, the *F*10.7, primarily a coronal emission, is not the best proxy to represent the Lyman α irradiance.

6. Physical Differences Between Models and Observations

In this section a solar irradiance proxy model is compared to a model that is based on the distribution of solar surface features. Our motivation for this comparison is to better characterize the capability of a solar proxy for predicting solar irradiance variations. For example, we show that the Mg C/W index is not as good a proxy for the Lyman α irradiance (which is primarily emitted from the transition region) as it is for radiation emitted from the chromosphere.

Lean and Skumanich [1983] established that at least three components are needed to model the Lyman α irradiance. They defined these components as quiet Sun, active network, and plages. The contribution to the total Lyman α irradiance was computed using estimated areas and intensities of each structure type. Plage areas were measured using ground-based Ca II K images [*Swartz and Overbeek*, 1971]. The active network area was a modeled value based on the estimated decay rate of active regions and the estimated area of the total photospheric network. The quiet Sun area was based on the distribution of Ca II K intensities over the solar disk.

Motivated by *Lean and Skumanich*'s [1983] three-component model, advances in computer processing speed, and the availability of large numbers of high-quality solar spectroheliograms at various wavelengths, *Worden et al.* [1998, 1999a] sought to determine how solar surface structures contribute to Ca II K (chromospheric) and He II 30.4-nm (transition region) irradiance variability. In both studies it was found that an additional component, enhanced network, significantly contributes to the irradiance emergent from the upper photosphere through the transition region. They also found that "active network" did not significantly contribute to Ca II K solar cycle irradiance variability but did significantly contribute to the solar cycle variability of the He II 30.4-nm irradiance. Before continuing with this analysis, it is useful to better characterize these different structures.

As noted by *Harvey and White* [1999], there are no universally accepted, unique nomenclature for the range of magnetic structures formed on the solar surface. For example, on a single solar intensity image it is difficult to separately identify a decayed plage, which may incorporate a decaying sunspot, from enhanced network. In addition, there is essentially no difference between enhanced network and active network at the smaller length scales. The following definitions for "plage," "enhanced network," "active network," and "quiet Sun" are referenced from previous work and adapted for modeling the solar UV irradiance.

1. A "plage" is the bright faculae associated with a photospheric, magnetic bipolar active region. Active region sizes range from 20,000 km to 100 Mm [*Schrijver*, 1988, and references therein]. After an active region emerges onto the surface, various surface processes, such as differential rotation, meridional flow, flows from supergranular convection cells, and chance encounters between other magnetic flux elements [e.g., *Leighton*, 1964; *Schrijver*, 1989;

Wang et al., 1991; Worden and Harvey, 2000], act to fragment and disperse an active region's magnetic flux.

2. The cancelation of magnetic flux along the neutral line appears to separate the active region into two different regions [*Schrijver*, 1989, *Worden and Harvey*, 2000]. Each region is primarily of one or other magnetic polarity. Sunspots have mostly dissipated, and supergranular convection is no longer completely suppressed within the region [*Zwaan*, 1987, and references therein]. However, the resulting structure is still large, compact, and bright in intensity images [*Worden et al.*, 1998]. These particular structures are defined as "enhanced network" [*Zwaan*, 1987; *Wang* and *Zirin*, 1991].

3. Supergranular convection cells form randomly on the surface, have diameters between 15,000 and 24,000 km [*Hagenar, et al.*, 1997; *Berrilli et al.*, 1998], and deform or dissipate approximately every 24 to 48 hours [*Singh et al.*, 1994; *Wang* and *Zirin*, 1991]. The flows associated with supergranular convection cells merge and fragment magnetic concentrations [e.g., *Schrijver et al.*, 1997; *Leighton*, 1964]. Although supergranular convection cells appear to be suppressed in active regions and mildly suppressed in enhanced network [*Zwaan*, 1987, *Wang and Zirin*, 1991], the flows associated with supergranular cells can still chew small-scale (lengths of ~15,000 km) magnetic flux concentrations from the edges of these larger, compact regions and disperse them across the Sun in a random walk manner [*Leighton*, 1964; *Schrijver* 1989]. These small-scale, bright features originating from active regions are called "active network" by *Lean and Skumanich* [1983] and *Skumanich et al.* [1984]. Like the enhanced network, they are primarily of one magnetic polarity. In addition, the migration of the active network to the poles is thought to be responsible for reversing the magnetic polarity of the polar fields every solar cycle [*Leighton*, 1964].

4. What is tentatively called the "quiet Sun" is a mixture of many things. Because the flows inside supergranular convective cells sweep magnetic flux to the cell boundaries, the cell interiors are nonmagnetic or weakly magnetic. As a result, the emergent radiance from supergranular cell interiors is not likely associated with magnetic fields [*Worden et al.*, 1999b; *Lites et al.*, 1999] and therefore does not significantly vary on solar cycle time scales [*Worden et al.*, 1999b; *Lean et al.*, 1998]. The magnetic fields associated with enhanced intensities at the cell boundaries (the photospheric network) have many sources including the magnetic intranetwork, ephemeral regions, and active network. The intranetwork are small bipoles with typical length scales of 1000 to 5000 km [e.g., *Solanki*, 1993]. It is thought that the amount of flux from the intranetwork does not vary with the solar cycle, because the intranetwork is likely formed near the surface [*Petrovay and Szakaly*, 1993]. However, the number of ephemeral regions, for example, magnetic bipoles with length scales of ~30,000 km [*Harvey and Martin*, 1973], and active network both vary with the solar cycle. Because much of the background magnetic network originates from sources that vary with the solar cycle, the irradiance measured during solar cycle minimum could be different for different solar cycles. It would therefore be incorrect to equate the solar minimum irradiance with a "quiet Sun" irradiance. However, the quiet Sun radiance is likely to be constant over the solar cycle and to have both magnetic and nonmagnetic components. For example, the irradiances of stars in a Maunder Minimum state (the irradiance is effectively constant over their expected equivalent stellar dynamo period) are found to have magnetic and nonmagnetic components (S. H. *Saar et al.*, manuscript in preparation, 2000).

In section 6.1 we compare a proxy model to a model that approximates the variation of these different solar structures with the solar cycle. In order to facilitate this comparison we coarsely group these multiple structures into three structures. The plage and enhanced network are combined into a single "plage" structure because these two structures are primarily responsible for the 27-day period seen in ultraviolet irradiance variations [*Worden*, 1996]. The quiet Sun irradiance is presumably some equilibrium value if the solar dynamo were turned off. The active network is the third component. Smaller ephemeral regions are incorporated as active network, and larger ephemeral regions are incorporated into the "plage" component.

6.1. Relationship of Long-Term and Short-Term Variations to Plage and Active Network Components

The three-component model of the irradiance E can conceptually be represented as the following:

$$E = E_Q\left[1+\left(C_N-1\right)f_N+\left(C_P-1\right)f_P\right]. \tag{3}$$

The f variables represent the summation of the fractional area of each component, and the C coefficients are the average contrast (ratio) between the component's radiance and the quiet Sun radiance. The subscripts Q, N, and P are for the quiet Sun, active network, and plage components, respectively. The center-to-limb variation is weighted with the contrasts (C_N and C_P), which are assumed to be effectively constant over the solar cycle [*Worden et al.*, 1998]. This three-component model is similar to *Lean and Skumanich*'s [1983] model and *Worden*'s [1996] model. *Lean and Skumanich* [1983] used the f_P to be the plage area derived from Ca II K images and the f_N to be the plage result smoothed over seven solar rotations and lagged by one rotation. *Worden* [1996] developed a similar model but derived both the plage and active network areas directly from Ca II K images. *Worden et al.* [1998] describe the processes and results of extracting the plage and active network areas from Ca II K images. Their analysis showed that the active regions (their plage and enhanced network components) had a strong 27-day variation, whereas the active network component barely had any 27-day variation. They further showed that the Ca II K contrast of the plage and active network did have a reasonably constant value over two solar cycles with a variation of 8 and 2% from its average for the plage and active network, respectively.

The three-component proxy model used here (equation (1)) was motivated by *Lean and Skumanich*'s [1983] and *Worden*'s [1996] models, but the components were selected differently to use the more readily available full-disk proxies. The sacrifice for a simpler, easier to use model is the loss of the direct link to the physical source of the emissions, namely, the plage and active network regions. Relating the different models represented by (1a) and (3) yields the following relationships:

$$E = E_{\min}\left[1+\frac{C_L}{E_{\min}}\left(P_{81}-P_{\min}\right)+\frac{C_S}{E_{\min}}\left(P-P_{81}\right)\right], \tag{4a}$$

$$E_2 = E_Q \begin{Bmatrix} 1+\left[\left(C_N-1\right)f_N+\left(C_P-1\right)f_{P\_81}\right] \\ + \left(C_P-1\right)\left(f_P-f_{P\_81}\right) \end{Bmatrix}, \quad (4b)$$

$$\text{short term} \equiv \frac{C_S}{E_{\min}}\left(P-P_{81}\right)=\left(C_P-1\right)\left(f_P-f_{P\_81}\right), \quad (4c)$$

$$\text{long term} \equiv \frac{C_L}{E_{\min}}\left(P_{81}-P_{\min}\right)=\left(C_N-1\right)f_N+\left(C_P-1\right)f_{P\_81}. \quad (4d)$$

Equation (4a) is (1a) rewritten with the condition that $E=E_{min}$ when $P=P_{81}=P_{min}$ in order for (1a) to look more like (3). Equation (4b) is (3) rewritten to look more like (1a) with the condition that the active network does not have any short-term variations. Then the similar terms in (4a) and (4b) are used to derive the relationship of short-term and long-term variations between the two different models. Therefore the short-term variation is equivalent to the short-term variation of the plage component. However, the long-term variation is a combination of the variation of both the active network and plage components. The short-term and long-term parameters C_S and C_L can be further reduced when the proxy is also modeled like (3):

$$P = P_{\min}\begin{Bmatrix} 1+\left[\left(C_{NP}-1\right)f_N+\left(C_{PP}-1\right)f_{P\_81}\right] \\ +\left(C_{PP}-1\right)\left(f_P-f_{P\_81}\right) \end{Bmatrix}, \quad (5a)$$

$$C_S = E_{min}\frac{\left(C_P-1\right)}{\left(C_{PP}-1\right)}, \quad (5b)$$

$$C_L = E_{min}\frac{\left(C_N-1\right)f_N+\left(C_P-1\right)f_{P\_81}}{\left(C_{NP}-1\right)f_N+\left(C_{PP}-1\right)f_{P\_81}} = E_{min}\frac{\left(C_N-1\right)K+\left(C_P-1\right)}{\left(C_{NP}-1\right)K+\left(C_{PP}-1\right)}, \quad (5c)$$

$$\frac{C_L}{C_S}=\frac{1+K\left(C_N-1\right)/\left(C_P-1\right)}{1+K\left(C_{NP}-1\right)/\left(C_{PP}-1\right)}. \quad (5d)$$

The proxy contrast ratios are labeled with the subscripts of *NP* and *PP* for the active network and plage contrast ratios, respectively. The long-term parameter is also further simplified using the assumption that the active network area is proportional to the 81-day-smoothed plage area; that is, $f_N = K f_{P\_81}$. *Lean and Skumanich* [1983] used a similar assumption in modeling the active network area, and the He II 30.4-nm images indicate that this assumption is reasonable with a K value of ~1 [*Worden et al.*, 1999a]. The relation of the long-term and short-term coefficients to the active network and plage contrasts is shown in (5d).

With these relationships established the physical differences between the long-term and short-term coefficients can be examined. One fundamental question to answer is "should emissions have the same short-term and long-term variations relative to a proxy?" From (5), there are only two conditions for which the short-term and long-term parameters can be the same. One condition for $C_L = C_S$ is that the active network is not seen in the proxy or in the emission being modeled, that is, $C_{NP} = C_N = 1$. While the contrast for the active network is small for most UV chromospheric and coronal emissions, the active network does contribute ~10-20% for these emissions [*Worden*, 1996]. Therefore this condition is not a realistic case. The other condition for $C_L = C_S$ is that the ratio of the active network contrast to the plage contrast be the same for the proxy and the emission being modeled, that is, $(C_{NP}\text{-}1)/(C_{PP}\text{-}1) = (C_N\text{-}1)/(C_P\text{-}1)$. As will be shown in section 6.4, this condition appears to occur for cases where the proxy and the emission are emitted at similar temperatures (altitudes) within the solar atmosphere. If neither of these two conditions is meet, then the long-term variation parameter is expected to be different than the short-term variation parameter. From (5) the long-term variation is predicted to be larger than the short-term variation if the active network contrast is more important for the emission than for the proxy; that is, . $(C_{NP}\text{-}1)/(C_{PP}\text{-}1) < (C_N\text{-}1)/(C_P\text{-}1)$. The opposite is also expected; the long-term variation is predicted to be smaller if the active network contrast is more important for the proxy than for the emission.

Another fundamental question to answer is "how instrument calibrations effect the differences between the short-term and long-term variations relative to a proxy?" Although our model represented in (1) is fit using linear regression, one can obtain very similar results by fitting the irradiance's long-term and short-term variations separately. In particular, the slope from the linear fit of the 81-day-smoothed proxy to the 81-day-smoothed irradiance is the long-term variation contrast, and the slope from the linear fit of the short-term proxy (P-P_{81}) to the short-term irradiance (E-E_{81}) is the short-term variation contrast. With this approach, the relation of the long-term contrast to the short-term contrast has the following relationship:

$$\frac{C_L}{C_S}=\frac{\left(E_{81}-E_{\min}\right)/\left(P_{81}-P_{\min}\right)}{\left(E-E_{81}\right)/\left(P-P_{81}\right)} = \frac{\left(E_{81}-E_{\min}\right)}{\left(E-E_{81}\right)}\frac{\left(P-P_{81}\right)}{\left(P_{81}-P_{\min}\right)}. \quad (6)$$

The ratio of the long-term to the short-term contrast is therefore insensitive to any systematic errors for the irradiance or proxy; that is, systematic offsets are canceled. For this reason, this ratio will be used in the following sections to examine the differences between various emissions and the proxies. However, a time-varying degradation function for either the irradiance or the proxy instrument would affect the long-term contrast more than the short-term contrast. A measurement sequence from one solar minimum to the next solar minimum would be beneficial in validating an instrument's degradation function. Because the solar minimum values for the proxies have very similar values, the degradation function for the irradiance instrument is the primary concern. In lieu of this verification for SOLSTICE, we will assume that the SOLSTICE degradation function is not an important factor for the ratio of the long-term to the short-term contrast, because the SOLSTICE degradation is believed to be accurate to a few percent.

6.2. Similarities Between the Mg Proxy and Chromospheric Emissions

The variation of the chromospheric emissions shows the greatest similarity to the variation of the Mg proxy, that is, $C_L \approx C_S$ when the Mg proxy is used for modeling the chromospheric emissions. Three SOLSTICE examples of this

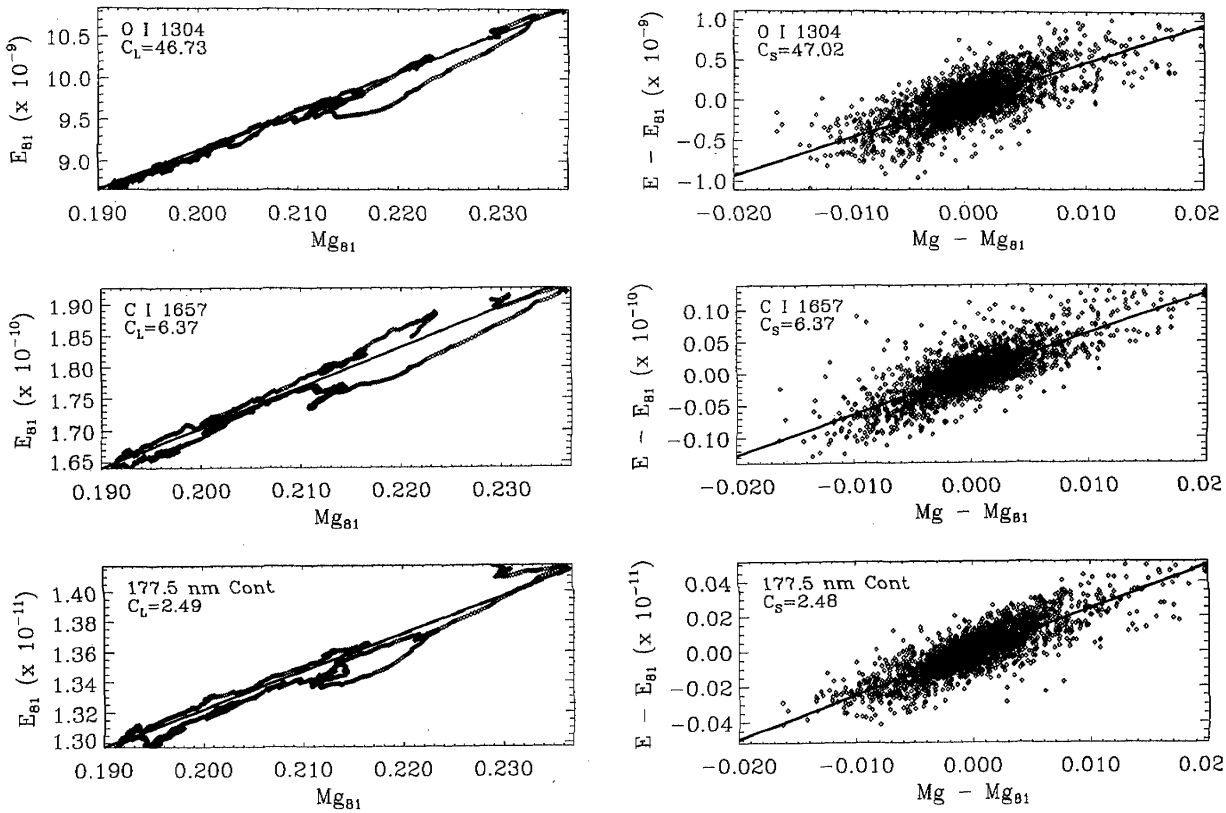

Figure 10. Chromospheric modeling with the Mg proxy. The long-term variation contrast C_L and short-term variation contrast C_S are shown as the solid lines for the SOLSTICE O I 130.4-nm emission, C I 165.7-nm emission, and 177-178 nm continuum. The dashed lines in the long-term plots (left side) are the slopes for the short-term variation, and the dashed lines in the short-term plots (right side) are the slopes for the long-term variation. These dashed lines are not discernible as they lie very close to the solid lines owing to the short-term and long-term variation contrasts are about the same value.

similarity are shown in Figure 10 for the O I 130.4-nm emission, the C I 165.7-nm emission, and the 177.5-nm continuum. In Figure 10 the long-term (81-day-smoothed) component and the short-term (daily minus the 81-day smoothed) component of each irradiance are compared to the long-term and short-term components of the Mg proxy. A linear fit is obtained for each component, and the slope of the fit is the variation coefficient. For these three emissions, the long-term parameter is within 5% of the short-term parameter. With the long-term parameter being very similar to the short-term parameter, a single linear relationship (two-component model) with the Mg proxy can be used, instead of a three component model, to predict the irradiance for most chromospheric emissions.

The Mg proxy is generated in the chromosphere at a temperature of ~6500 K [*Vernazza et al.*, 1981]. Thus the emissions formed between 6000 and 7000 K, such as the Ca II K emission and the far UV ($\lambda < 200$ nm) continuum, are likely to be similar to the Mg II k emission. From discussions above for (5) we expect that the ratio of the active network contrast to the plage contrast should be similar for most chromospheric emissions.

6.3. Differences Between the Mg Proxy and Transition Region Emissions

Unlike the chromospheric emissions, the transition region emissions have very different long-term and short-term variations relative to the Mg proxy. Three SOLSTICE examples of this difference are shown in Figure 11 for the He II 164.0-nm, N V 124.1-nm, and Lyman α emissions. The He II and N V emissions are emitted from the transition region with a excitation temperature of ~56,000 and ~200,000 K, respectively [*Vernazza et al.*, 1981]. The Lyman α emission is from both the chromosphere and transition region but has a peak in its source function near 40,000 K [*Woods et al.*, 1995; *Fontenla et al.*, 1991]. The difference between the long-term parameter and the short-term parameter is almost a factor of 2 for all of these transition region emissions.

The SOLSTICE irradiances between 119 and 182 nm are also modeled with the Mg proxy to examine any trends with excitation temperature. Both the SOLSTICE spectral irradiance in 1-nm intervals and the irradiances of several emissions extracted from the continuum are analyzed. The ratio of C_L/C_S is shown in Figure 12 as a function of wavelength and as a

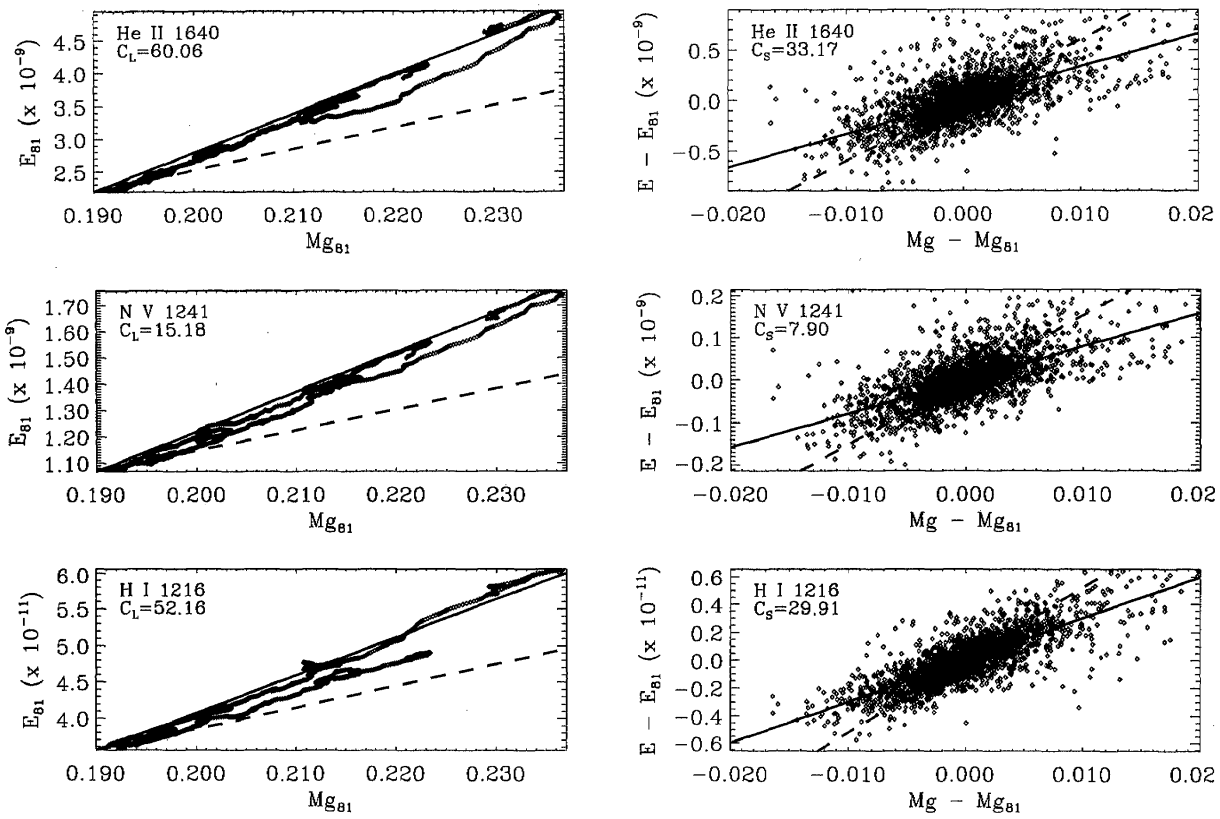

Figure 11. Transition region modeling with the Mg proxy. The long-term variation contrast C_L and short-term variation contrast C_S are shown as the solid lines for the He II 164.0-nm emission, N V 124.1-nm emission, and H I Lyman α emission. The dashed lines in the long-term plots (left side) are the slopes for the short-term variation, and the dashed lines in the short-term plots (right side) are the slopes for the long-term variation.

function of excitation temperature. The solid line in Figure 12 is the result for the SOLSTICE spectral irradiance in 1-nm intervals, and the diamond symbols are the results for the extracted emissions. Because it is not feasible to assign a temperature for the 1-nm spectrum that is a combination of continuum and emissions from different layers in the solar atmosphere, only the results from the extracted emissions are plotted versus temperature. For the 1-nm irradiances above 165 nm and near 130 nm, the ratio of C_L/C_S is ~1, thus suggesting that the chromosphere is the primary source for those wavelengths. The ratio of C_L/C_S as a function of temperature indicates a steady rise from 1 at the chromospheric temperature of 7000 K and then a fairly constant factor of ~1.8 for transition region emissions (temperatures between 20,000 and 400,000 K). Interestingly, the ratio of C_L/C_S for Lyman α is also a factor of 1.8, thus indicating that the Lyman α variability behaves more like transition region emissions than like chromospheric emissions.

6.4. Increase of Active Network Contrast and Plage Contrast in the Transition Region

With a long-term variation much larger than the short-term variation for the transition region emissions as compared to the chromospheric Mg proxy, the ratio of $(C_N\text{-}1)/(C_P\text{-}1)$ is expected to be larger for transition region emissions than for the chromospheric Mg proxy as indicated by (5d). This condition can be met if the active network contrast and plage contrast are both larger for the transition region emission than the contrasts for the Mg proxy. In particular, if both C_N and C_P increase by the same factor, the ratio of C_N/C_P will remain the same, but the ratio of $(C_N\text{-}1)/(C_P\text{-}1)$ will increase. Therefore the above transition region results indicate that the active network contrast and plage contrast should be larger for the transition region emissions than for the chromospheric emissions.

To verify this prediction, the ratio of $(C_N\text{-}1)/(C_P\text{-}1)$ is examined from contrast ratios derived from solar images and results derived from irradiance modeling. This ratio, as shown in Figure 13, ranges from 0.07 to 0.21 for the chromospheric emissions and from 0.26 to 0.42 for the transition region emissions. Although there is more spread in the values for this ratio, the ratio of $(C_N\text{-}1)/(C_P\text{-}1)$ has a similar trend in excitation temperature as the ratio of C_L/C_S. Therefore these results confirm that the active network and plage contrasts are larger for the transition region emissions than for the chromospheric emissions. These results also suggest that the active network should be more apparent in transition region images than in chromospheric or coronal images by a factor of ~2. *Reeves* [1976] showed that there is a peak in the network

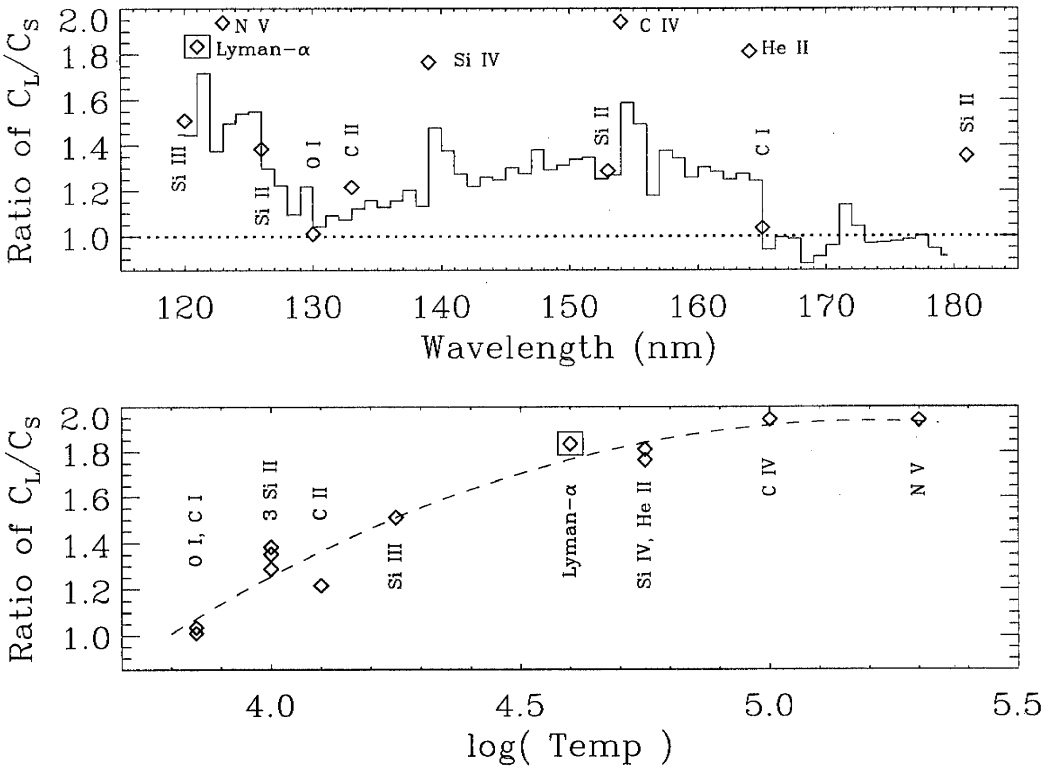

Figure 12. Ratio of C_L / C_S as a function of wavelength and excitation temperature. The long-term and short-term variation contrasts are derived using the Mg proxy with UARS SOLSTICE solar FUV irradiances. The solid line in the top panel is the contrast ratios for the SOLSTICE irradiances in 1-nm intervals on 0.5-nm centers. The diamonds are the contrast ratio for the brighter emissions extracted from the solar spectrum. Only the extracted emissions are assigned a excitation temperature. The dashed line in the bottom panel is a quadratic fit to the results.

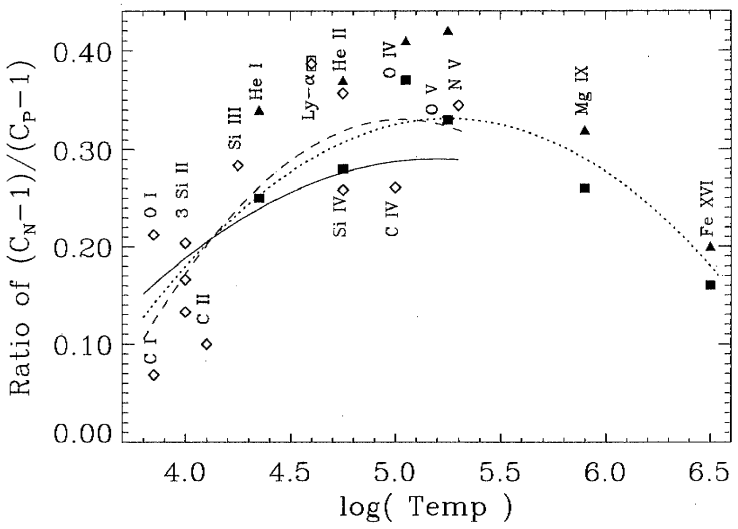

Figure 13. Ratio of *$(C_N$ -1)/(C_P -1)* as a function of excitation temperature. The diamonds represent the active network and plage contrast ratios that are derived from modeling the SOLSTICE FUV irradiance with active network and plage areas (Table 2 values). The dashed line is a quadratic fit to these results. The solid triangles and solid squares are the ratios that are derived from the histogram analysis and image analysis of Solar and Heliospheric Observatory (SOHO) Coronal Diagnostic Spectrometer (CDS) full-disk images (Table 1 values), respectively. The solid line is the predicted ratios using equation (5) and results in Figure 12. The dotted line is a quadratic fit for all of these results.

Table 1. Active Network and Plage Contrast Ratios From SOHO CDS Images[a]

Emission, nm	log(Temp)	Method	f_N	f_P	C_N	C_P	$(C_N-1)/(C_P-1)$
He II 30.4	4.75	HIST	0.17 ± 0.05	0.12 ± 0.05	1.60 ± 0.09	2.71 ± 0.56	0.37 ± 0.07
		IMAGE	0.36 ± 0.06	0.04 ± 0.03	1.73 ± 0.12	3.76 ± 0.87	0.28 ± 0.06
Fe XVI 33.5	6.50	HIST	0.10 ± 0.11	0.23 ± 0.24	1.75 ± 0.36	5.12 ± 2.25	0.20 ± 0.10
		IMAGE	0.25 ± 0.14	0.07 ± 0.06	2.37 ± 0.88	13.6 ± 8.9	0.16 ± 0.15
Mg IX 36.8	5.90	HIST	0.09 ± 0.06	0.10 ± 0.06	1.67 ± 0.25	3.15 ± 0.68	0.32 ± 0.11
		IMAGE	0.26 ± 0.09	0.05 ± 0.04	1.83 ± 0.19	4.60 ± 1.59	0.26 ± 0.08
O IV 55.5	5.05	HIST	0.22 ± 0.06	0.14 ± 0.03	1.81 ± 0.08	3.00 ± 0.36	0.41 ± 0.04
		IMAGE	0.44 ± 0.07	0.03 ± 0.02	2.00 ± 0.15	3.80 ± 0.73	0.37 ± 0.07
He I 58.4	4.35	HIST	0.18 ± 0.05	0.13 ± 0.06	1.67 ± 0.06	3.08 ± 0.69	0.34 ± 0.07
		IMAGE	0.36 ± 0.06	0.04 ± 0.04	1.83 ± 0.14	4.53 ± 1.32	0.25 ± 0.06
O V 63.0	5.25	HIST	0.21 ± 0.05	0.13 ± 0.03	1.82 ± 0.10	3.00 ± 0.43	0.42 ± 0.04
		IMAGE	0.42 ± 0.07	0.02 ± 0.02	1.98 ± 0.15	4.11 ± 0.92	0.33 ± 0.07

[a] The fractional area of the active network and plage (f_N and f_P) and the contrast ratios of the active network and plage (C_N and C_P) are derived from full-disk solar images using a "histogram" method (HIST) and an "image analysis" method (IMAGE). The values listed are the averages and the standard deviations for the 36 full-disk images taken by Solar and Heliospheric Observatory (SOHO) Coronal Diagnostic Spectrometer (CDS) from 1996 to 2000. See the text for clarification of the two methods.

contrast near a temperature of 150,000 K from the analysis of Skylab images at many wavelengths. Our results re-confirm these earlier results by *Reeves* [1976]. The remaining part of section 6.4 describes the derivation of the active network contrast and plage contrast values.

While there are several full-disk solar images from SOHO and Transport and Atmospheric Chemistry Near the Equator (TRACE) for a variety of chromospheric and transition region emissions, analysis of these images for average contrast ratios has not been published yet. So a uniform analysis at different wavelengths was performed using 36 full-disk solar images from the SOHO Coronal Diagnostic Spectrometer (CDS) [*Thompson and Carter*, 1998]. The active network and plage contrasts are listed in Table 1 for the He II 30.4-nm, Fe XVI 33.5-nm, Mg IX 36.8-nm, O IV 55.5-nm, He I 58.4-nm, and O V 63.0-nm emissions. These results, which are primarily representative of the transition region, were derived using two different techniques. One method used the intensity histogram technique, where the first Gaussian of the intensity histogram is assigned to be quiet Sun, the second Gaussain is assigned to be the active network, and the remaining intensity is assigned to be the plage. The other technique used the image analysis of intensity threshold and filling factor, such as by *Worden et al.* [1998], to identify the plage and active network components from the full-disk image. The center-to-limb variation is removed before the image analysis is performed. The histogram (HIST) method yielded larger plage fractional areas and thus smaller active network areas than the image analysis (IMAGE) method. Consequently, the plage contrasts are much smaller for the HIST method than for the IMAGE method. The resulting ratios of $(C_N-1)/(C_P-1)$ are, however, similar for both methods, but the ratios from the HIST method are systematically larger than the ratios from the IMAGE method. These CDS ratios are shown in Figure 13 as the solid triangles and solid squares. These CDS He II 30.4-nm results can be compared to the results for the EIT He II 30.4-nm images. *Worden et al.* [1999a] analyzed the EIT He II 30.4-nm images and found that the average active network contrast is 2.1 and that the average plage contrast is 4.0. Thus the ratio of $(C_N-1)/(C_P-1)$ for the EIT He II 30.4-nm emission is 0.37 and is in good agreement with the CDS ratios of 0.28 and 0.37.

The contrast ratios for the chromosphere, as derived from image analyses, are only derived from the ground-based Ca II K images. *Worden et al.* [1998] found for the Ca II K images that the average active network contrast is 1.3 and that the average plage contrast is 1.7. However, the extraction of the active network from the Ca II K images did not include the surrounding area as was done for the plage regions. Therefore the active network area is underestimated, which leads to the active network intensity contrast being overestimated [*Worden et al.*, 1998]. This overestimate for active network contrast might be as large as a factor of 2, so the ratio of $(C_N-1)/(C_P-1)$ for Ca II K is probably ~0.2 from *Worden et al.*'s [1998] image analysis. Using a different technique of the same Ca II K images, *Steinegger et al.* [1998] derive a plage contrast and active network contrast of 3.1 and 1.3, respectively, thus yielding a $(C_N-1)/(C_P-1)$ ratio of 0.15.

The active network and plage contrasts for Lyman α have also been studied. From Lyman α radiance measurements, *Schrijver et al.* [1985] obtained an average active network contrast of 1.7 from three quiet regions and an average plage contrast of 3.1 from 27 active regions. *Fontenla et al.*'s [1999] solar irradiance synthesis approach yields an average active network contrast of 3.0 and an average plage contrast of 6.1. This result used their model F as the active network, 90% of model H and 10% of model P as the plage, and 10% of model A, 80% of model C, and 10% of model E as the quiet Sun. These contrasts are different, mainly because the methods in defining the area of the active network or plage are different. In particular, the method that obtains larger areas yields smaller contrast ratios. Nonetheless, the ratio of $(C_N-1)/(C_P-1)$ for Lyman α ranges from 0.33 to 0.39 for these different contrast results.

With the lack of additional image analysis, the active network and plage contrast ratios derived from irradiance modeling by *Worden* [1996] are also examined. *Worden* [1996] models the SOLSTICE solar UV irradiances below 200 nm using the active network and plage areas derived from Ca II K images as the variables, and he determines the quiet Sun irradiance, active network contrast, and plage contrast as the model coefficients. He derives plage intensity contrast ratios that can be directly compared to plage contrast ratios derived from solar images. For example, he derived a Lyman α plage

Table 2. Active Network and Plage Contrast Ratios from Irradiance Modeling[a]

Emission, nm	log(Temp)	C_P	C_N	$(C_N-1)/(Cp-1)$	C_L/C_S
Si III 120.6	4.25	9.49	3.41	0.28	1.51
H I 121.6	4.60	6.70	3.21	0.39	1.84
N V 124.1	5.30	5.75	2.64	0.34	1.94
Si II 126.2	4.00	6.96	2.21	0.20	1.38
O I 130.4	3.85	4.21	1.68	0.21	1.01
C II 133.6	4.10	5.86	1.49	0.10	1.22
Si IV 139.8	4.75	6.99	2.55	0.26	1.77
Si II 153.0	4.00	6.35	1.71	0.13	1.29
C IV 155.0	5.00	4.67	1.96	0.26	1.94
He II 164.0	4.75	9.76	4.13	0.36	1.81
C I 165.6	3.85	3.08	1.14	0.07	1.04
Si II 181.3	4.00	4.79	1.63	0.17	1.35

[a] The active network contrast (C_N) and plage contrast (C_P) ratios are from modeling the UARS SOLar STellar Irradiance Comparison Experiment (SOLSTICE) irradiances [*Worden*, 1996]. The ratios of the long-term and short-term variation relative to the Mg proxy (C_L/C_S) are also listed.

contrast of 6.6, which is very similar to *Fontenla et al.*'s [1999] plage contrast result. The active network area is underestimated from the Ca II K image analysis [*Worden et al.*, 1998]; consequently, *Worden*'s [1996] active network contrast results are not directly comparable to active network contrast ratios derived from solar images. The active network contrast ratios from *Worden* [1996] are, however, relative to the true contrast ratios, so his values can be scaled uniformly at all wavelengths to match a reference contrast ratio. With his (C_a II K) Lyman α plage contrast being very similar to *Fontenla et al.*'s [1999] plage contrast, *Fontenla et al.*'s [1999] active network contrast is used as a reference to scale *Worden*'s [1996] active network contrast ratios so that the Lyman α active network contrast is 3.2. The plage contrast ratios and the scaled active network contrast ratios from *Worden*'s [1996] irradiance model are listed in Table 2. The ratio of $(C_N-1)/(C_P-1)$ for the He II 164-nm emission is 0.36 and is in very good agreement with the values from the He II 30.4-m image analysis. The ratios for the chromospheric O I and C I emission are also consistent with the value of 0.15-0.20 from the Ca II K image analysis.

All of these results for the active network and plage contrasts support that the transition region emissions have larger contrasts than those for chromospheric or coronal emissions. Therefore the long-term parameter is expected to be larger than the short-term parameter when modeling transition region emissions with chromospheric or coronal proxies. The ratio of $(C_N-1)/(C_P-1)$ is related to the ratio of C_L/C_S as shown in (5d) and is only one of the two relationships needed to understand the proxy models. The other proxy model relationship described by (5b) is that the short-term parameter C_S is proportional to the plage contrast (C_P-1). In general, the plage contrast increases going from the chromosphere into the corona. Therefore the better proxy for an emission will have both a similar plage contrast and a similar ratio of $(C_N-1)/(C_P-1)$. In other words, the better proxy for an emission will be from the same altitude and source region of the solar atmosphere. Deriving active network and plage contrast ratios from solar images at many other wavelengths is warranted to verify these ideas more conclusively.

6.5. Transition Region Irradiance Time Series Lag Behind Chromospheric Time Series

Because the ratio of $(C_N-1)/(C_P-1)$ is larger for transition region emissions than for chromospheric emissions, the active network contribution to the irradiance variability is expected to be larger for the transition region emissions than for the chromospheric emissions. Then with the active network evolving from the plage regions, the transition region irradiance time series are expected to lag behind the chromospheric time series. In other words, the active network lags behind the plage evolution by a period of a few months, so emissions that have a stronger network variability component, such as the transition region emissions, should lag behind emissions that have a weaker network component, such as the chromospheric emissions. This possibility for the Lyman α irradiance is checked by shifting its time series relative to the Mg proxy and by finding the time shift that gives the best proxy model fit. Because the solar rotation is a large component of variability, only time steps of a solar rotation (27 days) are tested. The lowest deviancies of the proxy model from the observations are found to be when both the SOLSTICE and SME Lyman α irradiances are lagged behind the Mg proxy by 54 days. The resulting proxy model comparisons with this 54-day lag of the Lyman α are shown in Figures 4b and 5b. There is a long-term drop of ~7% following solar minimum that is seen in both comparisons of the SOLSTICE and SME Lyman α irradiance to the Mg proxy model (Figures 4a and 5a). However, with the 54-day shift, this trend after solar minimum is mostly removed as shown in Figures 4b and 5b. This result supports the prediction that the transition region irradiance time series should lag behind a chromospheric proxy.

While the 54-day lag of the Lyman α irradiance improved its comparison to the Mg proxy, there remain some differences that could be caused by instrument artifacts. For SME the difference of ~5% for the first 2 years of the mission could be due to inaccuracies in the SME degradation function for the beginning of the mission. For SOLSTICE the difference of ~3% after 1998 perhaps implies that the SOLSTICE wavelength calibration, which was extrapolated past 1998, needs to be updated.

7. Improvements for Proxy Models

The Lyman α itself has been used as a proxy for modeling chromospheric and transition region emissions, such as in the EUV97 model [*Tobiska and Eparvier*, 1998]. The EUV97 model, as well as the other commonly used model by *Hinteregger et al.* [1981], is a two-component model; namely, the parameters are a constant coefficient and a contrast ratio of the emission's variability relative to the proxy's variability. These models also use a coronal proxy for the coronal emissions. The results in section 6.2 indicate that the two-component model approach is appropriate if the emission's source region, in temperature/altitude and in different types of active regions, is very similar to the proxy's source region. On the other hand, the results in section 6.3 indicate that the two-component model approach could fail by almost a factor of 2 if the proxy's source region is not consistent with the emission's source region. To better address these differences, we suggest two techniques for improving solar irradiance proxy models. One technique is to use long-term and short-

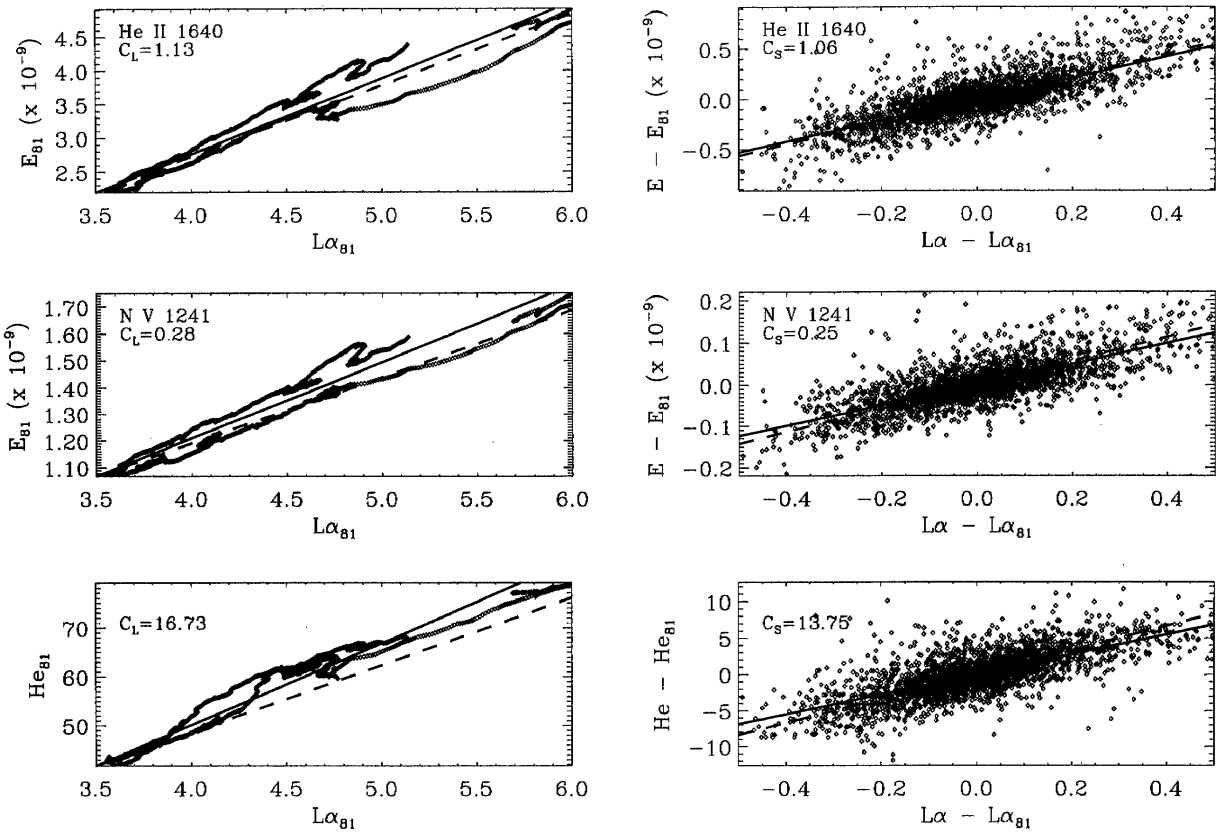

Figure 14. Transition region modeling with Lyman α. The long-term variation contrast C_L and short-term variation contrast C_S are shown as the solid lines for the He II 164.0-nm emission, N V 124.1-nm emission, and He EW proxy. The dashed lines in the long-term plots (left side) are the slopes for the short-term variation, and the dashed lines in the short-term plots (right side) are the slopes for the long-term variation.

term variables, such as is done in (1) with the 81-day-smoothed proxy as the long-term variable and the daily minus the 81-day-smoothed proxy as the short-term variable. A second technique is to include more classes of proxies besides the traditional chromospheric and coronal proxies. From this study, a separate proxy is needed for the chromosphere and transition region emissions. One solution is to use the Mg proxy for chromospheric emissions and to use our Lyman α composite time series as the proxy for transition region emissions. The transition region emissions of Si III and N V are compared to the Lyman α in Figure 14, and this comparison shows that their long-term and short-term variations relative to Lyman α are very similar. While either technique could improve the accuracy of a proxy model, the combination of both techniques would make the most significant improvement. An uncertainty of 10% or better seems possible for proxy models that use these techniques.

One method to estimate a solar instrument's degradation function is to assume that the long-term variation should be the same as the short-term variation relative to a proxy. For example, *Cebula et al.* [1998] used this method to estimate the degradation of the Solar Backscatter Ultraviolet (SBUV) instrument. On the basis of the results presented here, we caution against this instrument degradation technique unless the relation of the emission and proxy has been established to be the same for long-term and short-term variations. Fortunately, the measurements from the UARS SOLSTICE and SUSIM instruments, with their in-flight calibrations, should be able to establish these relations of solar UV irradiance to various proxies.

The primary product for most models of the Lyman α irradiance is the total line-integrated Lyman α irradiance, so the inclusion of the Lyman α line profile and how it varies could be another improvement for modeling the Lyman α irradiance. The partial redistribution of the Lyman α radiation in the chromosphere leads to a Lyman α profile that is normally reversed at line center, but some Solar Maximum Mission (SMM) measurements of the Lyman α radiance over plages have shown little or no line center reversal [*Fontenla et al.*, 1988]. With the Lyman α profile sometimes showing less line reversal over active regions, the profile of the Lyman α irradiance could change with solar activity. The Lyman α line profiles calculated for *Fontenla et al.*'s [1999] solar irradiance synthesis indicate that the plage intensity in the line center is ~50% more variable than the intensity in the wings. In other words, the Lyman α line center formed in the transition region is expected to be more variable than the Lyman α wings formed in the chromosphere. While SOLSTICE does not have high enough spectral resolution to measure any profile changes in the Lyman α 0.1-nm line core, *Woods et al.* [1995]

did show that the variability of the SOLSTICE Lyman α irradiance in the wings is about half of the line center variability and decreased steadily as the distance from line center increased. *Lemaire et al.* [1978], *Meier* [1995], and *Roussel-Dupré* [1982] are the primary references for high spectral resolution Lyman α profiles but without knowledge of whether the profile changes with solar activity. *Meier* [1995] also shows that the H I Lyman β profile is very similar to the Lyman α profile, but the remaining Lyman series lines can be represented by Gaussian functions with a width of ~0.03 nm. From more recent Lyman series measurements by SOHO SUMER, but excluding the Lyman α line, *Warren et al.* [1998] show that the Lyman series lines have stronger line reversal near the solar limb and that their line profiles change asymmetrically higher on the red side with increased intensity. The potential change in the Lyman α irradiance profile is an important issue for solar system studies of hydrogen abundance; therefore high spectral resolution measurements, to better than 0.02 nm, of the Lyman α irradiance are warranted during different levels of solar activity. In lieu of such observations, the Lyman β profiles from *Warren et al.* [1998] could be scaled, both in intensity and stretched for a wider profile, as a reasonable approximation for the Lyman α profiles.

8. Conclusions

A composite Lyman α time series is formed using the UARS SOLSTICE Lyman α measurements, AE-E and SME measurements adjusted to be consistent with the reference UARS measurements, and proxy model predictions to fill the data gaps and to extend the time series back to 1947. This Lyman α time series provides a continuous series between 1947 and 1999 without any data gaps for use in atmospheric research and for studying solar irradiance variations at other wavelengths. Our proxy models of the Lyman α irradiance used three components, instead of just two components, in order to predict the Lyman α irradiance more accurately. On the basis of the proxy model comparisons and uncertainties for the proxies and the UARS SOLSTICE Lyman α measurement, we estimate that these Lyman α irradiances have a 1-σ uncertainty of 10%. The amount of Lyman α variability is found to be similar to earlier results [i.e., *Vidal-Madjar*, 1977], but the magnitude of the Lyman α irradiance is ~70% higher than the early results reviewed by *Vidal-Madjar* [1977]. We attribute this discrepancy to instrument calibration differences.

In this report the differences between the AE-E, SME, and UARS data are assumed to be primarily due to instrument calibration differences to enable the combination of all three measurements into a single time series spanning five solar cycles. We expect that intrinsic solar variability may contribute secondary differences between the AE-E, SME, and UARS measurements. This cautionary note is especially important in light of the differences seen between the Lyman α irradiance and the proxy models. While most chromospheric emissions show a simple linear relation to the chromospheric Mg index, the Lyman α irradiance, as well as other transition region emissions, behaves differently. The differences between the Mg proxy and Lyman α irradiance are caused primarily by the active network contribution being more important for the Lyman α radiation than for the Mg proxy. Our results indicate that the active network and plage variability is a factor of ~2 larger for transition region emissions than for chromospheric or coronal emissions. The available proxies are primarily chromospheric and coronal emissions, whereas the Lyman α variability is manifested more in the transition region. A transition region proxy is therefore needed to improve the empirical proxy models of solar irradiance, and this composite Lyman α time series could serve as a proxy for other transition region emissions.

Acknowledgements. We are grateful to Barry Knapp, Giuliana de Toma, Marty Snow, Oran R. White, Cindy Russell, Brian Boyle, Mike Dorey, and Ann Windnagel for their assistance with and useful discussions about the SOLSTICE data set. We thank Bill Thompson for providing the SOHO CDS full-disk solar images. This research is supported by NASA grant NAG5-6850 to the University of Colorado and NASA contract NAS5-97179 (APL contract 774017, UCB SPO BS0059849) to Federal Data Corporation. The composite Lyman α time series, as shown in Figure 7, can be retrieved via anonymous ftp (account: anonymous; password: your e-mail address) from the "laspftp.colorado.edu" computer. The text file is called "composite_lya.dat" in the directory "pub/solstice/".

Janet G. Luhmann (editor) and the authors thank the referees for their assistance in evaluating this paper.

References

Barth, C. A., W. K. Tobiska, G. J. Rottman, and O. R. White, Comparison of 10.7 cm radio flux with SME solar Lyman alpha flux, *Geophys. Res. Lett.*, *17*, 571-574, 1990.

Berrilli, F., A. Florio, and I. Ermolli, On the geometrical properties of the chromospheric network, *Sol. Phys.*, *180*, 29-45, 1998.

Brasseur, G., and P. C. Simon, Stratospheric chemical and thermal response to long-term variability in solar UV irradiance, *J. Geophys. Res.*, *86*, 7343-7362, 1981.

Brueckner, G.E., K.L. Edlow, L.E. Floyd, J.L. Lean, and M.E. VanHoosier, The Solar Ultraviolet Spectral Irradiance Monitor (SUSIM) Experiment on board the Upper Atmosphere Research Satellite (UARS), *J. Geophys. Res.*, *98*, 10,695-10,711, 1993.

Canfield, L. R., R. G. Johnston, and R. P. Madden, NBS detector standards for the far ultraviolet, *Appl. Opt.*, *12*, 1611-1617, 1973.

Cebula, R. P., M. T. DeLand, and E. Hilsenrath, NOAA 11 Solar Backscatter Ultraviolet, model 2 (SBUV/2) instrument solar spectral irradiance measurements in 1989-1994, 1, Observations and long-term calibration, *J. Geophys. Res.*, *103*, 16,235-16,249, 1998.

de Boor, C., *A Practical Guide to Splines*, Chaps. 9-11, Springer-Verlag, New York, 1978.

Donnelly, R. F., D. F. Heath, J. L. Lean, and G. J. Rottman, Differences in the temporal variations of solar UV flux, 10.7-cm solar radio flux, sunspot number, and Ca-K plage data caused by solar rotation and active region evolution, *J. Geophys. Res.*, *88*, 9883-9888, 1983.

Donnelly, R. F., O. R. White, and W. C. Livingston, Solar Ca II K index and the Mg II core-to-wing ratio, *Sol. Phys.*, *152*, 69-76, 1994.

Fontenla, J., E. J. Reichmann, and E. Tandberg-Hanssen, The Lyman-alpha line in various solar features, I, Observations, *Astrophys. J.*, *329*, 464-481, 1988.

Fontenla, J. M., E. H. Avrett, and R. Loeser, Energy-balance in the solar transition region, 2, Effects of pressure and energy input on hydrostatic models, *Astrophys. J.*, *377*, 712-725, 1991.

Fontenla, J. M., O. R. White, P. A. Fox, E. H. Avrett, and R. L. Kurucz, Calculation of solar irradiances, I, Synthesis of the solar spectrum, *Astrophys. J.*, *518*, 480-499, 1999.

Foukal, P., What determines the relative areas of spots and faculae on sun-like stars ?, *Astrophys. J.*, *500*, 958-965, 1998.

Frederick, J. E., Chemical response of the middle atmosphere to changes in the ultraviolet solar flux, *Planet. Space Sci.*, *25*, 1-4, 1977.

Fukui, K., Anomalous increase of Lyman alpha flux during the solar maximum phase of cycle 21 observed by the AE-E satellite, *Environ. Res. Pap. 1051*, 20pp., U.S. Air Force, Hanscom Air Force Base, Mass., 1990

Hagenaar, H. J., C. J. Schrijver, and A. M. Title, The distribution of cell sizes of the solar chromospheric network, *Astrophys. J.*, *481*, 988-995, 1997.

Harvey, J. W., and W. C. Livingston, Variability of the solar He I 10830

Å triplet, in *Infrared Solar Physics*, edited by D. M. Rabin, J. T. Jefferies, and C. Lindsey, pp. 59-64, Kluwer Acad., Norwell. Mass., 1992.

Harvey, K. L., and S. F. Martin, Ephemeral active regions, *Sol. Phys.*, *32*, 389-402, 1973.

Harvey, K. L., and O. R. White, Magnetic and radiative variability of solar surface structures, I, Image decomposition and magnetic-intensity mapping, *Astrophys. J.*, *515*, 812-831, 1999.

Heath, D. F., and B. M. Schlesinger, The Mg 280-nm doublet as a monitor of changes in solar ultraviolet irradiance, *J. Geophys. Res.*, *91*, 8672-8682, 1986.

Hinteregger, H. E., K. Fukui, and B. R. Gilson, Observational, reference and model data on solar EUV from measurements on AE-E, *Geophys. Res. Lett.*, *8*, 1147-1150, 1981.

Hoegy, W. R., W. D. Pesnell, T. N. Woods, and G. J. Rottman, How active was solar cycle 22?, *Geophys. Res. Lett.*, *20*, 1335-1338, 1993.

Lawson, C. L, and R. J. Hanson, *Solving Least Squares Problems*, Chap.10 and 27, Prentice-Hall, Englewood Cliffs, N.J., 1974.

Lean, J. L., and A. Skumanich, Variability of the Lyman alpha flux with solar activity, *J. Geophys. Res.*, *88*, 5751-5759, 1983.

Lean, J. L., J. Cook, W. Marquette, A. Johannesson, and R. C. Willson, Magnetic sources of the solar irradiance cycle, *Astrophys. J.*, *492*, 390-401, 1998.

Leighton, R. B., Transport of magnetic fields on the Sun, *Astrophys. J.*, *140*, 1547-1562, 1964.

Lemaire, P., J. Charra, A. Jouchoux, A. Vidal-Madjar, G. E. Artzner, J. C. Vial, R. M. Bonnet, and A. Skumanich, Calibrated full-disk solar H I Lyman-α and Lyman-β profiles, *Astrophys. J.*, *223*, L55-L58, 1978.

Lites, B. W., R. J. Rutten, and T. E. Berger, Dynamics of the solar chromosphere, II, Ca II H_{2V} and K_{2V} grains versus internetwork fields, *Astrophys. J.*, *517*, 1013-1033, 1999.

Meier, R. R., Solar Lyman series line profiles and atomic hydrogen excitation rates, *Astrophys. J.*, *452*, 462-471, 1995.

Mount, G. H., and G. J. Rottman, Solar absolute spectral irradiance 1150-3173 Å: May 17, 1982, *J. Geophys. Res.*, *88*, 5403-5410, 1983.

Mount, G. H., and G. J. Rottman, Solar absolute spectral irradiance 118-300 nm: July 25, 1983, *J. Geophys. Res.*, *90*, 13,031-13,063, 1985.

Petrovay, K., and G. Szakaly, The origin of intranetwork fields: A small-scale solar dynamo, *Astron. Astrophys.*, *274*, 543-554, 1993.

Reeves, E. M., The EUV chromospheric network in the quiet Sun, *Sol. Phys.*, *46*, 53-72, 1976.

Rottman, G. J., Rocket measurements of the solar spectral irradiance during solar minimum, 1972-1977, *J. Geophys. Res.*, *86*, 6697-6705, 1981.

Rottman, G. J., T. N. Woods, and T. P. Sparn, Solar Stellar Irradiance Comparison Experiment 1, 1, Instrument design and operation, *J. Geophys. Res.*, *98*, 10,667-10,678, 1993.

Roussel-Dupré, D., Skylab observations of H I Lyman-α, *Astrophys. J.*, *256*, 284-291, 1982.

Roussel-Dupré, D., H I Lyman-α in the Sun: The effects of partial redistribution in the line wings, *Astrophys. J.*, *272*, 723-738, 1983.

Schrijver, C. J., Radiative fluxes from the outer atmosphere of a star like the Sun: A construction kit, Astron. Astrophys., *189*, 163-172, 1988.

Schrijver, C. J., The effect of an interaction of magnetic flux and supergranulation on the decay of magnetic plages, *Sol. Phys.*, *122*, 193 – 208, 1989.

Schrijver, C. J., C. Zwaan, C. W. Maxson, and R. W. Noyes, A study of ultraviolet and X-ray emissions of selected solar regions, *Astron. Astrophys.*, *149*, 123-134, 1985.

Schrijver, C. J., A. M. Title, A. A. van Ballegooijen, H. J. Hagenaar, and R. A. Shine, Sustaining the quiet photospheric network: The balance of flux emergence, fragmentation, merging, and cancellation, *Astrophys. J.*, *487*, 424-436, 1997.

Singh, J., B. S. Nagabhushana, G. S. D. Babu, and W. Uddin, Study of calcium-K network evolution from Antarctica, *Sol. Phys.*, *153*, 157-167, 1994.

Skumanich, A., J. L. Lean, W. C. Livingston, and O. R. White, The Sun as a Star: Three-component analysis of chromospheric variability in the calcium K line, *Astrophys. J.*, *282*, 776-783, 1984

Solanki, S. K., Smallscale solar magnetic fields: An overview, *Space Sci. Rev.*, *63*,1-15, 1993.

Steinegger, M., J. A. Bonet, M. Vazquez, and A. Jimenez, On the intensity thresholds of the network and plage regions, *Sol. Phys.*, *177*, 279-286, 1998.

Swartz, W. E., and R. Overbeek, *Rep. 373 (E)*, Ionos. Res. Lab., Penn. State Univ., University Park, 1971.

Tapping, K. F., Recent solar radio astronomy at centimeter wavelengths: The temporal variability of the 10.7-cm flux, *J. Geophys. Res.*, *92*, 829-838, 1987.

Thompson, W., and M. Carter, EUV full-Sun imaging and pointing calibration of the SOHO Coronal Diagnostic Spectrometer, *Sol. Phys. 178*, 509-521, 1998.

Tobiska, W. K. and F. G. Eparvier, EUV97: Improvements to EUV irradiance modeling in the soft x-rays and FUV, *Sol. Phys., 177*, 147-159, 1998.

Tobiska, W. K., W. R. Pryor, and J. M. Ajello, Solar hydrogen Lyman-α variation during solar cycles 21 and 22, *Geophys. Res. Lett.*, *24*, 1123-1127, 1997.

Van Hoosier, M., J. Bartoe, G. Brueckner, and D. Prinz, Absolute solar spectral irradiance 120 nm – 400 nm (results from the Solar Ultraviolet Spectral Irradiance Monitor-SUSIM-experiment on board Spacelab 2), *Astrophys. Lett. Commun.*, *27*, 163-168, 1988.

Vernazza, J. E., E. H. Avrett, and R. Loeser, Structure of the solar chromosphere, III, Models of the EUV brightness components of the quiet Sun, *Astrophys. J. Suppl. Ser.*, *45*, 635-725, 1981.

Vidal-Madjar, A., The solar spectrum at Lyman-alpha 1216 Å, *in The Solar Output and Its Variation*, edited by O. R. White, pp. 213-236, Colo. Assoc. Univ. Press, Boulder, 1977.

Wang, H., and H. Zirin, Magnetic flux transport of decaying active regions and enhanced magnetic network, *Sol. Phys.*, *131*, 53-68, 1991.

Wang, Y.-M., N. R. Sheeley Jr., and A. G. Nash, A new solar cycle model including meridional circulation, *Astrophys. J.*, *383*, 431-442, 1991.

Warren, H.P., J. T. Mariska, and K-Wilhelm, High resolution observations of the solar hydrogen Lyman lines in the quiet Sun with the SUMER instrument on SOHO, *Astrophys. J. Suppl.*, *119*, 105-120, 1998.

Woods, T. N., and G. J. Rottman, Solar EUV irradiance derived from a sounding rocket experiment on 10 November 1988, *J. Geophys. Res.*, *95*, 6227-6236, 1990.

Woods, T. N., and G. J. Rottman, Solar Lyman α irradiance measurements during two solar cycles, *J. Geophys. Res.*, *102*, 8769-8779, 1997.

Woods, T. N., G. J. Rottman, O. R. White, J. Fontenla, and E. H. Avrett, The solar Lyα line profile, *Astrophys. J.*, *442*, 898-906, 1995.

Woods, T. N., *et al.*, Validation of the UARS solar ultraviolet irradiances: Comparison with the ATLAS 1 and 2 measurements, *J. Geophys. Res.*, *101*, 9541-9569, 1996.

Woods, T., G. Rottman, C. Russell, and B. Knapp, In-flight degradation results for the UARS SOLSTICE instrument, *Metrologia, 35*, 619-623, 1999.

Worden, J. R., A three component proxy model for the solar far ultraviolet irradiance, dissertation, Univ. of Colo., Boulder, 1996.

Worden, J. R., and J. Harvey, An evolving synoptic magnetic flux map: Implications for the distribution of photospheric magnetic flux, *Sol. Phys.*, in press, 2000.

Worden, J. R., O. R. White, and T. N. Woods, Evolution of chromospheric structures derived from Ca II K spectroheliograms: Implications for solar ultraviolet irradiance variability, *Astrophys. J.*, *496*, 998-1014, 1998.

Worden, J. R., T. N. Woods, W. M. Neupert, and J.-P. Delaboudmiére, Evolution of chromospheric structures: How chromospheric structures contribute to the solar He II 30.4 nanometer irradiance and variability, *Astrophys. J.*, *511*, 965-975, 1999a.

Worden, J. R., J. Harvey, and R. Shine, Bright chromospheric grains and the magnetic intranetwork, *Astrophys. J.*, *523*, 450-457, 1999b.

Zwaan, C., Elements and patterns in the solar magnetic field, *Annu. Rev. Astrophys.*, *25*, 83-111, 1987.

G. J. Rottman and T. N. Woods, Laboratory for Atmospheric and Space Physics, University of Colorado, 1234 Innovation Dr., Boulder, CO 80303. (tom.woods@lasp.colorado.edu)

W. K. Tobiska, Federal Data Corporation, Jet Propulsion Laboratory, Pasadena, CA 91109.

J. R. Worden, Atmospheric and Environmental Research Inc., Cambridge, MA 02139.

(Received February 16, 2000; revised June 16, 2000; accepted July 7, 2000.)